Advanced Functional Materials

ADVANCED FUNCTIONAL MATERIALS
www.afm-journal.de

RESEARCH ARTICLE OPEN ACCESS

An Engineered Living Material With Pro-Angiogenic Activity Inducible by Near-Infrared Light

Anwesha Chatterjee[1,2] | Stefanie S. M. Meier[3] | Sara Trujillo[1] | Andreas Möglich[3] | Shrikrishnan Sankaran[1]

[1]INM - Leibniz Institute for New Materials, Saarland University, Saarbrücken, Germany | [2]Chemistry Department, Saarland University, Saarbrücken, Germany | [3]Department of Biochemistry, University of Bayreuth, Bayreuth, Germany

Correspondence: Sara Trujillo (sara.trujillomunoz@leibniz-inm.de) | Andreas Möglich (andreas.moeglich@uni-bayreuth.de) | Shrikrishnan Sankaran (shrikrishnan.sankaran@leibniz-inm.de)

Received: 17 November 2025 | **Revised:** 6 March 2026 | **Accepted:** 9 March 2026

Keywords: alginate | angiogenesis | engineered living materials (ELM) | *Escherichia coli* nissle 1917 | HUVECs | NIR photobiomodulation

ABSTRACT

Impaired angiogenesis is a central barrier in the treatment of chronic and deep tissue wounds, preventing progression through the normal healing cascade. While the combination of near infrared (NIR) photobiomodulation and pro-angiogenic growth factors has shown synergistic therapeutic benefit, the clinical translation of growth factor therapy is hindered by high cost, instability, and the need for localized dosing to avoid aberrant vasculature. Peptidomimetics such as the VEGF-derived QK peptide offer a more stable and predictable alternative, but still require a means for localized, tunable presentation. Here, we establish an engineered living material-based delivery system that responds to clinically relevant NIR light to produce and release a QK-Fusion protein directly at the target site. The probiotic *Escherichia coli* Nissle 1917 was engineered with an 800 nm-responsive optogenetic circuit and encapsulated within an optimized alginate core–shell hydrogel that ensures biocontainment while allowing controlled outward diffusion of the secreted peptide. The released peptide remains non-cytotoxic, capable of binding extracellular matrix analogs, and promotes angiogenesis in endothelial cultures and the chick chorioallantoic membrane assay. We thus establish a strategy for developing engineered living materials toward remote-controlled angiogenic stimulation.

1 | Introduction

Healing of complex dermal defects remains a major clinical challenge because the native cascade of hemostasis, inflammation, proliferation, and remodeling is often derailed by infection, metabolic disorders, or poor vascularization. Photobiomodulation with red and near-infrared (NIR, 650–950 nm) light has emerged as a non-invasive strategy to re-establish this cascade: NIR light penetrates several millimeters through tissue, boosts mitochondrial ATP production, dampens excessive inflammation, and accelerates collagen deposition, all while avoiding thermal damage [1]. In pre-clinical rodent and porcine models, pulsed 810 or 830 nm lasers shortened closure times and markedly increased granulation tissue and capillary density [2, 3], and first-in-human studies now report faster epithelialization of venous leg ulcers [4].

Angiogenesis is a decisive bottleneck in tissue regeneration, and several groups therefore pair NIR illumination with exogenous pro-angiogenic cues. For example, topical recombinant epidermal growth factor (EGF) delivered alongside 830-nm light closed a deep burn in a human patient within five treatments [5] and, in a delayed tooth-replantation model, adjunctive basic fibroblast growth factor (FGF) plus 808-nm light administration improved periodontal regeneration and curbed root resorption compared with either therapy alone [6]. Despite this promise, translation of recombinant growth factors is hampered by two long-standing obstacles. First, their picomolar potency means that even

modest overdosing induces aberrant, leaky vasculature, oedema, or tumor-like lesions, necessitating tight local concentration control [7]. Second, large-scale production, purification, and cold-chain logistics render full-length proteins prohibitively expensive [8]. Furthermore, these growth factors are susceptible to enzymatic degradation and hydrolysis in the body, thereby requiring large initial doses [9]. Vascular endothelial growth factor (VEGF), for instance, costs orders of magnitude more per milligram than standard biologics yet shows a narrow therapeutic window and off-target effects when chronically overexpressed [10].

Material scientists and protein engineers have tackled these hurdles along two complementary lines. First, smart delivery vehicles have been advanced to control growth-factor dosing. These vehicles comprise either micro-/nanoparticles, core–shell hydrogels, or photo-responsive matrices and provide on-demand, localized release while minimizing systemic spill-over. In one study, for instance, gold nanorod-conjugated liposomes embedded in collagen hydrogels enabled the release of both VEGF and platelet-derived growth factor (PDGF) at different NIR wavelengths [11]. In a different strategy, injectable black phosphorous nanosheet hydrogels released molecules upon exposure to 808 nm NIR light [12]. Furthermore, hydrogels containing MXenes (2D metal carbides with photothermal properties) functioned as effective photothermal platforms, releasing growth factors like VEGF or EGF under controlled conditions by transforming NIR light into localized heat [13, 14]. Second, peptidomimetics—small fragments of the growth factors—are being developed to reduce the cost of growth factor therapies, as they are smaller and cheaper to produce. These synthetic analogs simulate either the key functional or structural domains of the native proteins while providing high stability, reduced immunogenicity, and improved bioavailability [15]. Some examples include the SPPEPS sequence (TGF-β mimic) for promoting chondrogenesis [16], single-chain tandem macrocyclic peptides (STaMPtides) as hepatocyte growth factor (HGF) receptor agonists [17], and VEGF peptide mimetics, which support vascularization [18, 19]. Among VEGF peptidomimetics, the QK peptide—derived from the α-helical region of $VEGF_{165}$—has been widely studied for its ability to stimulate endothelial cell proliferation and capillary formation. Similar to native VEGF, QK demonstrates better angiogenic activity when immobilized onto the extracellular matrix, increasing its chemotactic activity [18].

Engineered living materials (ELMs) now promise to unite these advances in a single platform. By embedding genetically programmed microbes inside a biocompatible matrix, ELMs enable continuous, self-renewing synthesis of therapeutic payloads whose timing and dose are set by user-defined stimuli. We recently demonstrated the concept by entrapping blue-light-responsive *E. coli* in Pluronic F127 hydrogels to secrete collagen-binding QK on cue. Subsequent reports using alginate or gelatin matrices, probiotic lactobacilli, and diverse inducible triggers underline the versatility and translational potential of ELMs [20, 21].

Here, we build on these foundations and report an NIR-light-regulated, pro-angiogenic ELM tailored for deep-tissue wounds. Our system harnesses the clinically proven probiotic *Escherichia coli* Nissle 1917 (EcN), endowed with our recently developed NIR-light-responsive optogenetic circuit, to synthesize and secrete a QK-based fusion protein only when illuminated with 800 nm light. The bacteria are confined within core–shell alginate beads whose nanoporous shell prevents cell escape yet allows protein diffusion. We show that these ELMs can be precisely controlled, with secretion switched ON and OFF or tuned by light intensity, and that the secreted QK is functional, non-cytotoxic, sufficient to induce angiogenic network formation in 2D cultures of endothelial cells and in the complex, in vivo-like environment of the chick chorioallantoic membrane assay.

2 | Results and Discussion

2.1 | Engineering *E. coli* Nissle 1917 for Light-Responsive Secretion

For this study, we used our recently developed optogenetic circuit *Av*NIRusk that controls bacterial gene expression by NIR light [22]. The light signal is translated by an engineered two-component system into a gene expression output. Specifically, the first component is a chimeric histidine kinase consisting of the light sensor module from the bacterial phytochrome *Agrobacterium vitis* (*Av*PCM) and the catalytic domains of the histidine kinase FixL from *Bradyrhizobium japonicum*. In the presence of NIR light, the chimeric histidine kinase phosphorylates the second component, the response regulator FixJ from *B. japonicum*. In its phosphorylated state, FixJ binds to the FixK2 promoter and initiates gene expression. All these components and the gene of interest are encoded on the single *Av*NIRusk plasmid (Figure 1a). As an initial validation, we tested the expression of the fluorescent reporter *Ds*Red in *E. coli* Nissle 1917 (EcN), which was upregulated a hundred-fold under NIR light with minimal basal expression (Figure S1a–c). We further performed a dose-response experiment using *Ds*Red fluorescence as output with varying NIR intensities to determine the optimal power level for the maximal activation of the system (Figure S1d).

Building upon this platform, we replaced the original reporter protein with a 28 kDa therapeutic fusion protein containing the VEGF-mimetic QK peptide (13 amino acids). This fusion protein also harbors the signal peptide of the native OmpA protein, called *ompa*, to facilitate secretion, a thermostable nuclease from *Staphylococcus aureus*, termed as nuclease A (NucA) domain for enzymatic assays [23], an SmBiT tag (11 amino acids) for luminescent quantification [24], and a collagen-binding domain (CBD; 10 amino acids) for the protein to bind to the extracellular matrix [25] (Figure 1a). This fusion protein is hereafter referred to as QK-Fusion. The sequences of the individual domains are listed in Table S1.

Although *E.coli* is a preferred host for recombinant protein production, it exhibits limited efficiency in secreting heterologous proteins due to constraints in the native export systems [26, 27]. Particularly in EcN, high secretion can lead to periplasmic burden and growth trade-offs [28]. While recent efforts have explored signal-peptide optimization and heterologous secretion systems to improve extracellular release, secretion of fully functional recombinant proteins from EcN remains modest. To address this bottleneck, the NucA domain was incorporated not only as a reporter for quantification via DNase assays but also to

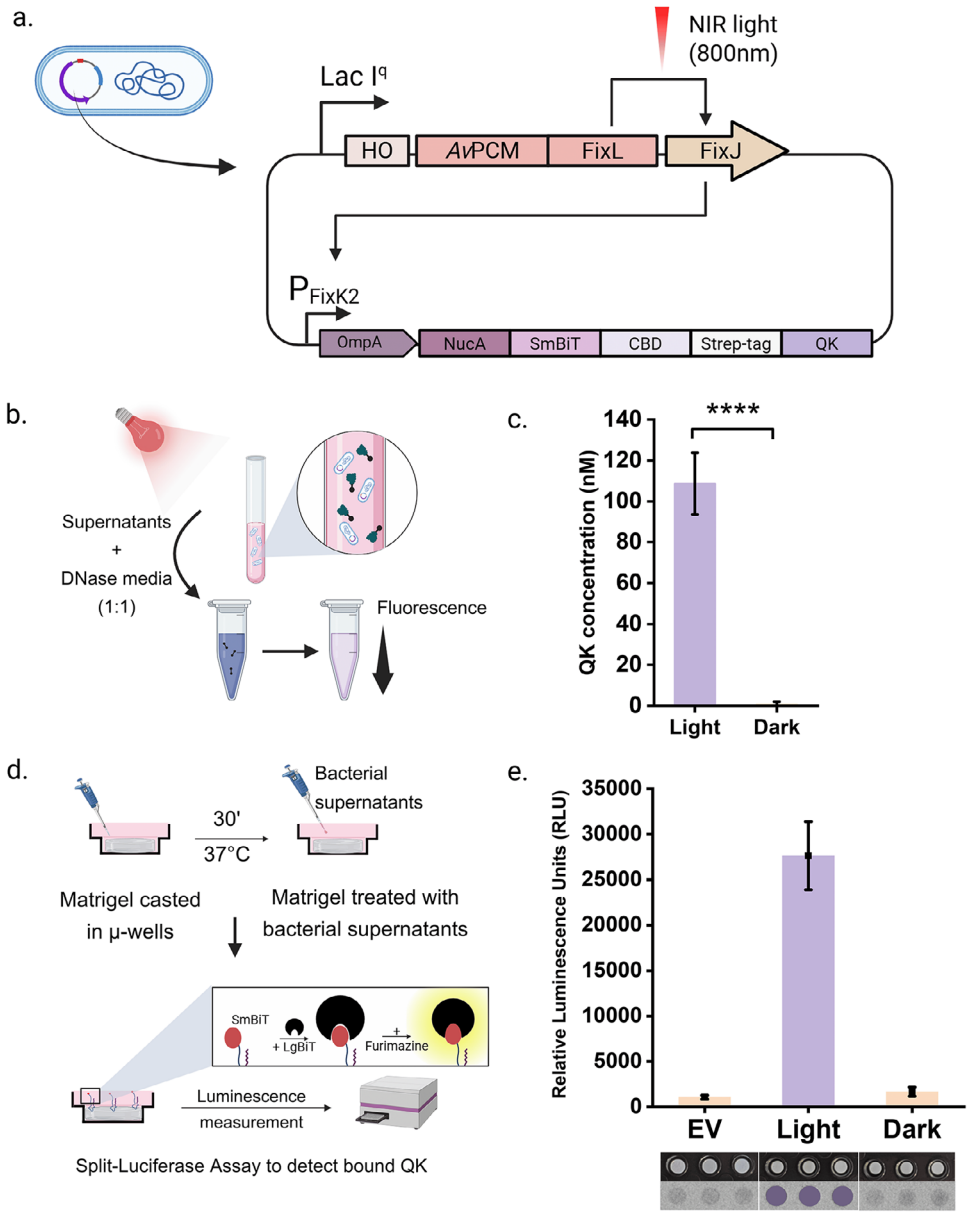

FIGURE 1 | Genetic design and characterization of the near-infrared light-responsive bacteria. (a) Architecture of the *Av*NIRusk plasmid for NIR-light-dependent secretion in bacteria. The engineered light-switchable two-component system is constitutively expressed as a tricistronic operon from the lacIQ promoter. Said operon contains in sequential order a heme oxygenase for provision of the biliverdin chromophore; a chimeric histidine kinase comprising the photosensor of the bacterial phytochrome from *Agrobacterium vitis* (*Av*PCM) linked to the catalytic domains of *B. japonicum* FixL; and the cognate response regulator FixJ from *B. japonicum*. In NIR light, FixJ is phosphorylated, binds to the FixK2 promoter, and thereby initiates the expression of the therapeutic QK-Fusion protein. Said protein contains the OmpA signal peptide for secretion, the nuclease A from *Staphylococcus aureus*, and the SmBiT tag for enzymatic and luminescent measurements, respectively. The collagen-binding domain (CBD) enables binding to the extracellular matrix, and the QK peptide is a VEGF-mimic. (b) Schematic of Nuclease Assay using culture supernatants. Supernatants from light and dark bacterial cultures were mixed 1:1 with DNase media. Upon incubation, QK-Fusion proteins containing NucA cleaved the DNA causing a loss of fluorescence comparable to the enzymatic activity. (c) Quantification of secreted QK protein under NIR light vs dark conditions. Nuclease assay confirmed strong light-dependent secretion from engineered bacteria (QK concentration in nM), with minimal background under dark conditions. Data represent mean ± SD. (d) Schematic of collagen binding assay. Growth-factor-reduced Matrigel was cast in µ-slides and incubated with bacterial supernatants for QK-fusion to bind to the collagen via the collagen-binding domain. Binding was detected via Split–Luciferase Assay. (e) Measurement of Collagen-bound QK using split-luciferase assay. High luminescence signals were detected only in light-induced samples, indicating efficient secretion and collagen binding of QK. Empty vector (EV) and dark conditions showed a negligible signal. Data shows mean ± SD. (Bottom) Luminescence images of EV, light, and dark conditions on a 96-well plate taken with a ChemiDoc MP imaging system (Bio-Rad, Germany).

increase the hydrophilicity of the fusion protein, which improved secretion efficiency by roughly 460-fold (Figure S2a).

Following the construction of the *Av*NIRusk-QK-Fusion plasmid and transforming it into EcN to create the EcN NIR-QK-Fusion strain, we evaluated the ability of the engineered bacteria to produce and secrete the fusion protein in a NIR light-responsive manner. To this end, log-phase cultures of these bacteria were incubated either under 800 nm NIR light or dark conditions at 37°C overnight. Culture supernatants were collected, and the quantity of secreted proteins was determined by measuring the enzyme activity of NucA through its ability to degrade DNA stained with a fluorescent dye (Figure 1b). The NucA activity was quantified by measuring the fluorescence intensity in solution, and the normalized values were converted to concentration values (nM) with a standard curve (Figure S2b). Supernatants from NIR-induced cultures exhibited 137-fold higher DNase activity than those kept in the dark, confirming that the engineered construct was both successfully expressed and secreted in a NIR light-dependent manner (Figure 1c). For visual detection of the enzyme activity, we also put the EcN on DNase agar plates containing an indicator dye and kept them either in the dark or under NIR light. The plates under NIR light showed a halo of discoloration around the bacteria, confirming that the secreted peptide is capable of degrading DNA. The halo gets bigger by increasing the intensity of incident NIR light (Figure S3).

As stated earlier, the activity of the QK peptide relies on its immobilization to the extracellular matrix, and hence, we assessed the binding capability of the secreted fusion protein. To test this, culture supernatants collected from EcN NIR-QK-Fusion grown under NIR light or dark conditions were incubated on matrigel-coated wells and, after washing, immobilization of the protein was visualized via the split luciferase assay. A ChemiDoc MP imaging system was used to image luminescence in the wells, and the intensity was quantified using a microplate reader (Figure 1d). Supernatants derived from light-induced cultures showed robust luminescence signals, both visually and quantitatively, in contrast to cultures grown in the dark and a negative control. These results confirm that the secreted engineered protein can bind to the matrix in a light-dependent manner (Figure 1e).

2.2 | ELM Fabrication and Characterization

To translate the genetically engineered bacterial system into a functional and biocompatible ELM, the EcN NIR-QK-Fusion strain was encapsulated within an alginate hydrogel in a core–shell format. The bead architecture closely follows the "protein eluting alginate with recombinant lactobacilli" (PEARL) platform which exhibited containment of recombinant Lactobacilli and controlled the release of secreted proteins but failed to contain *E. coli* [21]. Thus, modifications to the encapsulation method were developed to ensure containment of EcN.

Encapsulation was carried out in a two-step gelation process. A bacterial–alginate mixture was dropped into calcium chloride to form the core beads, with Alcian Blue added for visualization. These beads were then individually immersed in a second alginate solution and once again crosslinked in calcium chloride to form a uniform shell around the core (Figure 2a). In the macroscopic images, the bead core appears as a uniform blue sphere, while the core plus shell bead is visibly larger, with a transparent outer layer surrounding the core. The corresponding microscopy images give a general view of how the bead looks after 2 days of bacterial growth in the bead (Figure 2b). The bacteria grew into a dense collection of colonies within the core, while not penetrating the shell. Regarding light-responsiveness, fluorescent colonies were observed only in the beads that were irradiated with NIR light (Figure 2c).

To reach a formulation that balanced protein release with containment of *E. coli*, we first replicated the published PEARL parameters using EcN in LB medium but observed considerable amount of bacterial leakage within 16 h of encapsulation. While the PEARL platform evidently sufficed for *Lactobacillus*, it could not contain the fast growing and highly motile EcN. Thus, we systematically optimized the system to achieve containment of EcN. We varied one key parameter at a time such as $CaCl_2$ concentration, alginate concentration, crosslinking duration, media composition or bacterial growth phase prior to encapsulation over multiple experimental sets. Table S2 and Figure S4 summarize the empirical workflow that guided the rational formulation of the final core–shell system used in this study. Increasing crosslinking duration to 4 h and switching from LB to M199 media in the core reduced bacterial escape significantly while supporting secretion. With the escape problem under control, we focused on maximizing protein secretion. We noticed that on increasing alginate concentration, protein secretion decreased further. We hypothesized that the positively charged QK-Fusion might be getting trapped in the negatively charged alginate matrix under higher alginate concentrations or suboptimal crosslinking conditions. Guided by this, we adjusted to lower alginate concentration in the core (2 wt.%) and shell (1.5 wt.%) and increased $CaCl_2$ for shell crosslinking (8 wt.%) which improved both protein release and matrix stability. Although no single factor ensured containment on its own, all adjustments together led to the final core–shell system that was stable, reproducible and well-suited for use as an ELM platform. The final formulation (summarized in Table 1) consisted of a 2 wt.% alginate core (bacteria in M199 media supplemented with 0.4% w/v glucose, OD_{600} = 0.3–0.5) surrounded by a 1.5 wt.% alginate shell, with the core crosslinked in 6 wt.% $CaCl_2$ for 30 min and the shell in 8 wt.% $CaCl_2$ for 4–5 h.

Table 1 summarises the final optimized formulation that reproducibly generated ~4 mm beads. In this system, EcN was successfully retained within the optimized core–shell architecture designed to restrict bacterial escape while permitting diffusion of secreted peptides. To evaluate long-term containment, supernatants from individual beads were plated on LB-agar supplemented with kanamycin throughout 10 days. Most beads showed no detectable bacterial growth throughout the study, with only occasional leakage observed at later time points (Day 10), likely arising from manual error during bead fabrication (Figure S5a). In parallel, the beads maintained robust structural integrity under physiologically representative conditions (M199 culture medium, 37°C, pH ~ 7.4, with negligible mass loss, retaining 94% ± 2.5% of their initial wet mass with no observed structural disintegration (Figure S5b).

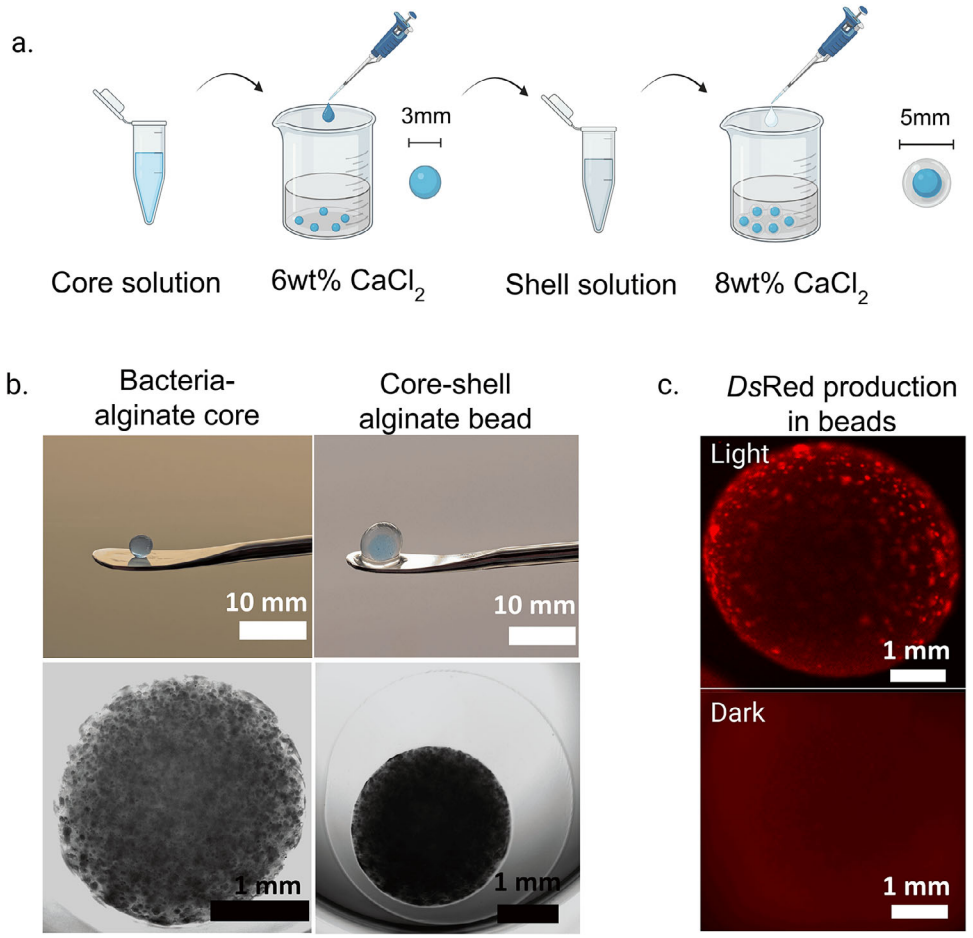

FIGURE 2 | Encapsulation and characterization of engineered EcN in core–shell alginate beads. (a) Schematic of the two-step fabrication process of the alginate beads. A bacterial–alginate mixture (1:2) was first crosslinked in 6 wt.% $CaCl_2$ to form the core, followed by a second encapsulation in 1.5 wt.% alginate and crosslinking in 8 wt.% $CaCl_2$ to form the shell. (b) Macroscopic and brightfield microscopy images showing bead morphology. Top: Macroscopic images of a bacteria-loaded alginate core (left) and a complete core–shell bead (right) taken immediately after crosslinking. Bottom: Brightfield microscopy pictures showing bacterial growth inside the core (left) and core–shell (right) after 24 h of incubation. (c) Fluorescence microscopy of encapsulated EcN expressing *Ds*Red Express2 under NIR light (top) and dark (bottom), confirming light-dependent protein production within the bead.

TABLE 1 | Final optimized formulation for fabrication of alginate core–shell ELMs.

Core conc^n	Crosslinking time (core)	Media in core	Shell conc^n	Crosslinking time (shell)
2 wt.% alginate	30 mins	M199-Kan + 0.4% w/v Glu	1.5 wt.% alginate	4 h

2.3 | Dynamic Light-Controlled Secretion From ELMs

With the encapsulation method established, we proceeded to assess if the system remained inducible and capable of secretion. First, we encapsulated *E. coli* Nissle 1917 harboring an AvNIRusk vector driving *Ds*Red expression and exposed some of the resultant beads to NIR light while keeping the remainder in the dark. The beads exposed to NIR light showed distinct red fluorescent colonies under the microscope, while those kept in the dark did not (Figure 2c). This confirmed that the bacteria remained alive inside the hydrogel and were viable enough to respond to NIR light and produce the target protein. After demonstrating viability and light-responsiveness, we evaluated whether the system was able to produce and secrete the QK-Fusion protein. Secretion of the protein from the beads was quantified via NucA assay with bead supernatants. After 24 h of induction, the concentration of the secreted protein was 30 ± 7 nM. In contrast, the surrounding medium from uninduced beads (incubated in the dark) displayed negligible NucA activity (Figure 3a).

We tested the same supernatants in a collagen-binding assay to evaluate whether the secreted peptide retained its ability to bind to collagen. To this end, we collected the surrounding media from induced, uninduced, and control beads, incubated them on Matrigel, and confirmed binding via Split–Luciferase Assay.

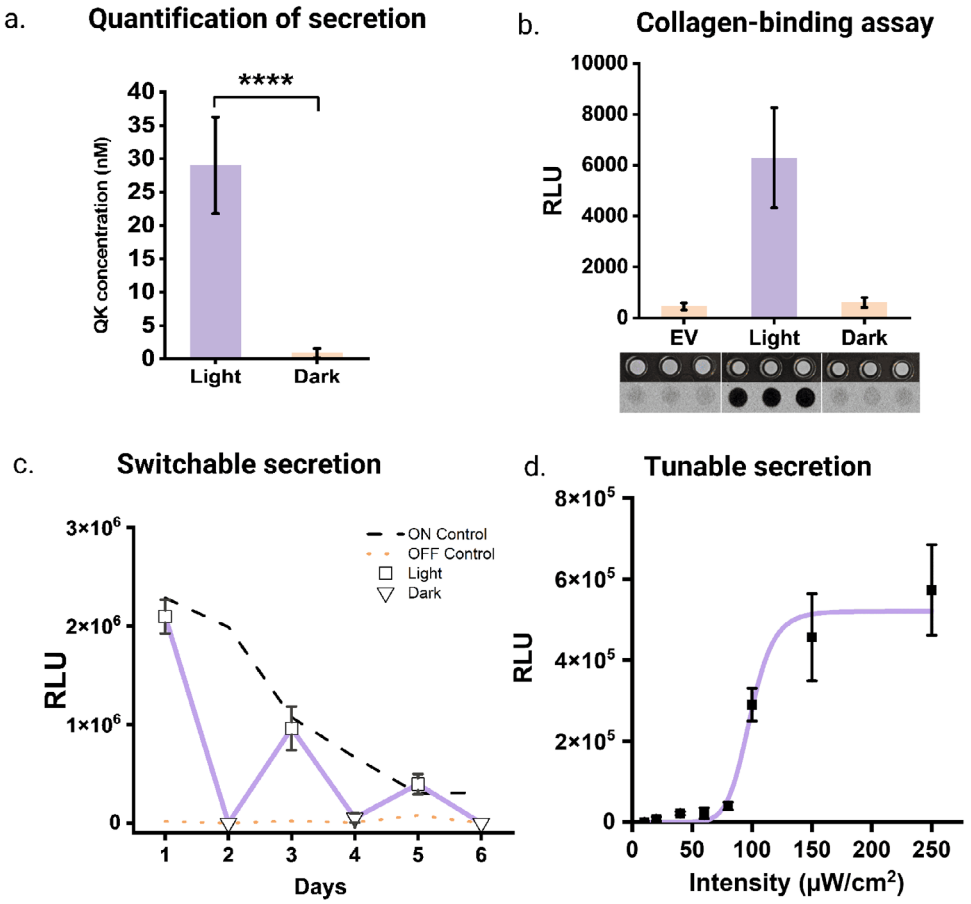

FIGURE 3 | Secretion dynamics and light-responsive control of ELMs. (a) Quantification of secreted QK-Fusion protein from ELMs under light and dark conditions with the Nuclease Assay. (b) Measurement of QK-Fusion bound to the collagen matrix via Split-Luciferase Assay. Luminescence signals were detected only in light-induced bead supernatants, indicating efficient secretion and collagen binding of QK. Empty vector (EV) and dark conditions showed a negligible signal. Data shows mean ± SD. (Bottom) Luminescence images of EV, light, and dark conditions on a 96-well plate taken with a ChemiDoc MP imaging system. (c) Switchability of QK-Fusion secretion from ELMs across six days under alternating light and dark conditions. Cultures were induced with NIR light (ON) or kept in the dark (OFF), and luminescence was measured from supernatants each day. A consistent light–dark response was observed, confirming switchable secretion. QK-Fusion secreting beads kept in constant light (ON) and dark (OFF) for six days were used as controls. (d) Intensity-dependent tunability of QK-Fusion secretion. QK-Fusion secreting beads were subjected to different intensities of 800 nm NIR light. Data were fitted to the Hill equation, yielding $RLU_{max} = 5.2 \times 10^5$, $I_{50} = 98.5\,\mu W\,cm^{-2}$, and $n = 9.98$.

Supernatants from NIR-induced beads showed strong luminescence signals, whereas the uninduced ones showed minimal binding, comparable to the empty vector control. These results indicate that QK-Fusion secreted by the encapsulated bacteria remained intact and functional, retaining its collagen-binding capability after production and release into the surrounding medium (Figure 3b).

To further evaluate the dynamic control of these ELMs, we next tested if our system could reversibly turn secretion ON and OFF over multiple induction cycles. The ELMs were divided into three groups: one maintained under constant NIR illumination (ON), one kept permanently in the dark (OFF), and the third one subjected to alternating light and dark conditions every 24 h. Following each induction period, the surrounding media were analyzed using the Split–Luciferase assay, the medium was replenished, and the light/dark setting of the third group was inverted. The experiment showed clear and repeatable switching of QK-Fusion secretion. Beads exposed to NIR light showed a sharp increase of luminescence, reflecting active production and release of the QK-Fusion protein. When moved back to the dark, the luminescence values reached baseline levels, confirming that there was no detectable secretion in the dark. Switching the beads from dark to light once again caused a rise in signal. This alternating behavior continued over all six cycles, demonstrating that the secretion response was switchable. Nevertheless, a gradual decline in secretion was observed over successive NIR induction cycles including in the constant ON condition. We initially suspected that this decline might be due to loss of bacterial viability from nutrient depletion arising from prolonged encapsulation in the sub-optimal M199 media. To evaluate this possibility, alginate beads were dissolved in sodium citrate solutions, and viable bacteria were quantified through CFU analysis. The analysis confirmed that bacteria remained viable even after 6 months (Figure S6a,b). Furthermore, the recovered colonies, when re-cultured in planktonic conditions, could also be re-induced by NIR illumination with protein secretion comparable to fresh bacterial cultures (Figure S6c). In parallel, further optimization of media composition, aimed at improving bacterial fitness did not restore secretion levels,

suggesting that reduced viability alone could not explain the observed decline (Table S3). These observations indicate that the decrease in secretion does not originate from loss of cell viability. We then hypothesized that this decline could likely be due to a reduction in oxygen availability to the encapsulated bacteria, a commonly reported feature in alginate-based hydrogels [29–31]. This is also supported by our results in Figure 2c, where the fluorescent protein DsRed, which requires oxygen for the maturation of its fluorophore, is mainly expressed close to the periphery of the core. This lack of oxygen, in turn, can negatively impact the activation of the NIR optogenetic circuit itself, as the incorporated heme oxygenase required molecular oxygen for the conversion of heme to biliverdin, the chromophore necessary for phytochrome-mediated light activation [32]. To improve oxygen diffusion, modification of the alginate bead formulation, network structure, or dimensions could be explored in future studies. Nevertheless, throughout the experiment, the OFF-control group stayed at very low levels, confirming that secretion occurred only when triggered by NIR light (Figure 3c).

We next tested if the secretion from the ELMs was tunable with increasing intensity of NIR light. To confirm this, we exposed the ELMs to a range of intensities from 0 to 250 μW cm^{-2}. The secretion stayed negligible at low intensities but showed a steep increase beyond 80 μW cm^{-2} and plateaued around 150 μW cm^{-2} (Figure 3d). This response pattern resembles the previously reported dose response for NIR-responsive EcN producing *Ds*Red [22]. In that study, activation was triggered at somewhat lower light intensities, beginning around 20 μW cm^{-2} and reaching saturation near 50 μW cm^{-2}. The present shift to higher intensities for activation might be caused by a combination of factors including decreased penetration of light through dense bacterial colonies in the alginate beads compared to planktonic bacterial cultures, altered metabolic state of the confined bacteria, and slower diffusion of the secreted QK-Fusion protein through the alginate to the surrounding media. However, despite the lowered sensitivity, the light doses required for full system activation remain orders of magnitude below the maximum NIR-light intensity (~200 mW/cm^2) considered therapeutically safe [33–36]. In addition, lower sensitivity might even prove beneficial in therapeutic applications as it can mitigate unintended activation by low levels of ambient light. Taking together, we established that our ELMs can be switched ON and OFF at will, and the secretion can be tuned by adjusting the light intensity.

2.4 | Cytocompatibility of ELM Supernatants

Encouraged by the promising results, we proceeded to investigate the ability of the secreted QK-Fusion protein to drive angiogenic differentiation in human Umbilical Vein Endothelial Cells (HUVECs). Notably, HUVECs are well-established in vitro model cells for assessing behaviors such as migration, proliferation, and capillary network formation [37]. Before performing functional assays, we first examined whether the secreted QK-Fusion protein and other bacterial metabolites were toxic to the HUVECs. We incubated monolayer HUVEC cultures for 24 and 72 h with supernatants from induced cultures, ELMs, and empty vector strain-containing ELMs as a control. Cytocompatibility was assessed through complementary qualitative (live/dead staining) and quantitative assays (lactate dehydrogenase (LDH) assay and AlamarBlue assay) (Figure 4).

Live/dead staining performed after 24 and 72 h of supernatant treatment showed predominantly viable cells in both empty vector ELM and induced QK-Fusion ELM supernatants. This was comparable to the cells maintained in standard growth medium which served as a negative control for membrane damage (Figure 4a). Consistent with this, LDH release calculations showed about 80% cell viability across all treatment conditions, at both 24 and 72 h (Figure 4b). This was comparable to LDH released by untreated cells cultured in growth medium (negative control) and far lower than LDH released by cells lysed with Triton X-100 for complete membrane disruption and maximal cell death (positive control). Cell metabolic activity analysis with AlamarBlue showed no significant differences between treated and untreated cells after 24 h. At 72 h, the increase in metabolic activity points to cell proliferation over time for all conditions. Proliferation in treated cells happened at a slightly lower rate compared to the control, which could be due to a slightly lower availability of nutrients due to the presence of EcN. Cell viability remained high across all conditions, indicating sustained cytocompatibility of the ELM supernatants over prolonged exposure (Figure 4c). These findings confirm that neither QK nor the EcN metabolic byproducts have any adverse effect on HUVECs, and thus, the ELM supernatants are cytocompatible over prolonged exposure.

2.5 | Network Formation Assay

Having ruled out cytotoxic effects, we next tested whether the secreted QK-Fusion could drive angiogenesis via a 2D network formation assay [37]. To this end, we used growth-factor-reduced Matrigel in μ-well plates to form a basement membrane-like layer. On the polymerized Matrigel, supernatants from bacterial culture and ELMs were pipetted and incubated at 37°C overnight for the QK-Fusion to bind to the matrix. The following day, serum-starved endothelial cells were seeded onto the gels, where they adhered and rearranged to form network-like structures. The network formation was then analyzed by brightfield microscopy after 4–6 h (Figure 5a).

As this is a highly dynamic process, we first tracked cellular arrangement over time by time-lapse brightfield microscopy. Cells treated with supernatants from negative control, positive control, and NIR-induced QK beads were followed over 20 h while capturing still images every 20 min. The full videos are shown in Supporting Information (Movies S1–S3). The positive control condition triggered a rapid rearrangement of the endothelial cells into well-defined networks with big lumens, which continued to mature over time. The networks formed in this condition were stable over 12 h. On the other hand, the negative control condition showed little to no organization. Small groups of cells reorganized in an unstable manner, which still shows the suitability of Matrigel to host endothelial cells even in the growth factor-depleted version. Interestingly, the endothelial cells treated with supernatants from light-induced ELMs formed well-defined networks that closely resembled the networks formed by positive controls in terms of morphology and stability over time (stable up to 7 h).

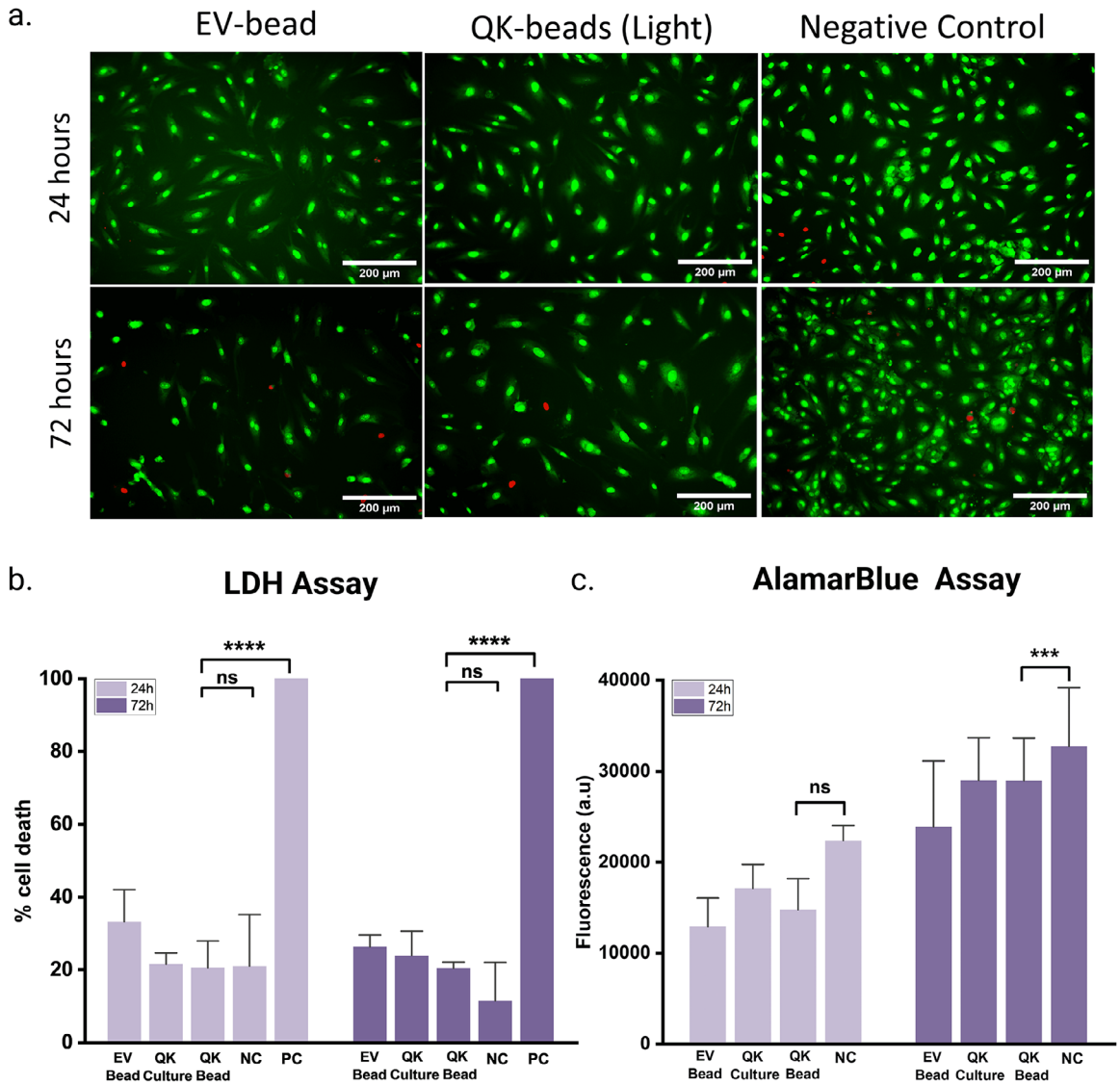

FIGURE 4 | Cytocompatibility assessment of ELMs and bacterial cultures on HUVECs. (a) Representative fluorescent images of the live/dead staining of HUVECs after 24 h (top) and 72 h (bottom) of treatment with ELM supernatants and negative control (live (green): SYTO9, dead (red): PI). (b) LDH assay showing percent cell death in HUVECs, 24 and 72 h after treatment with supernatants from QK-Fusion producing bacterial cultures (QK-Culture) and beads (QK-Bead) under NIR-illumination, compared to positive control (PC), negative control (NC), and empty vector (EV). (c) AlamarBlue assay showing metabolic activity of HUVECs, 24 and 72 h after treatment with supernatants from QK-Fusion producing bacterial cultures (QK-Culture) and beads (QK-Beads) under light conditions, compared to growth medium as negative control (NC) and empty vector (EV). Both assays indicate no significant cytotoxicity from supernatants. Graphs are shown as data ± S.D. ($N = 3$, $n \geq 3$).

From the time-lapse results, we established that network formation occurs during the first 4–6 h. Building upon this, we extended our analysis to incorporate multiple conditions and assess network morphology via endpoint microscopy. We compared the potential pro-angiogenic effects of the secreted QK-Fusion from culture and ELM bead supernatants in light and dark conditions, together with the empty vector and positive and negative controls (Figure 5). The microscopy images revealed distinct morphological differences between the experimental groups (Figure 5b). The positive control presented elongated networks, with connected and thick vessel-like structures, while the negative control showed scattered cells without proper connected vessels. In contrast, supernatants from both culture and ELMs incubated under NIR light supported robust network formation closely resembling the positive control. In comparison, supernatants from culture and ELMs in the dark-state seemed to support limited networks in a few samples but were largely comparable to the negative control.

Quantitative analysis of network formation was performed using Angiotool in ImageJ (Figure 5c–f). We focused on four parameters to effectively assess angiogenic behavior across the different conditions. Vessel Area (in percentage), which measures the fraction of the image occupied by segmented vessels, and Total Vessel Length, defined as the cumulative length of all skeletonized vessel segments, Total number of vessels, corresponding to the number of discrete vessel segments, and finally, Junction Density, which quantifies the number of branch points per unit area. Combined, these four measures reflect the coverage of the network, the length of the vessels, and the amount of branching. All together

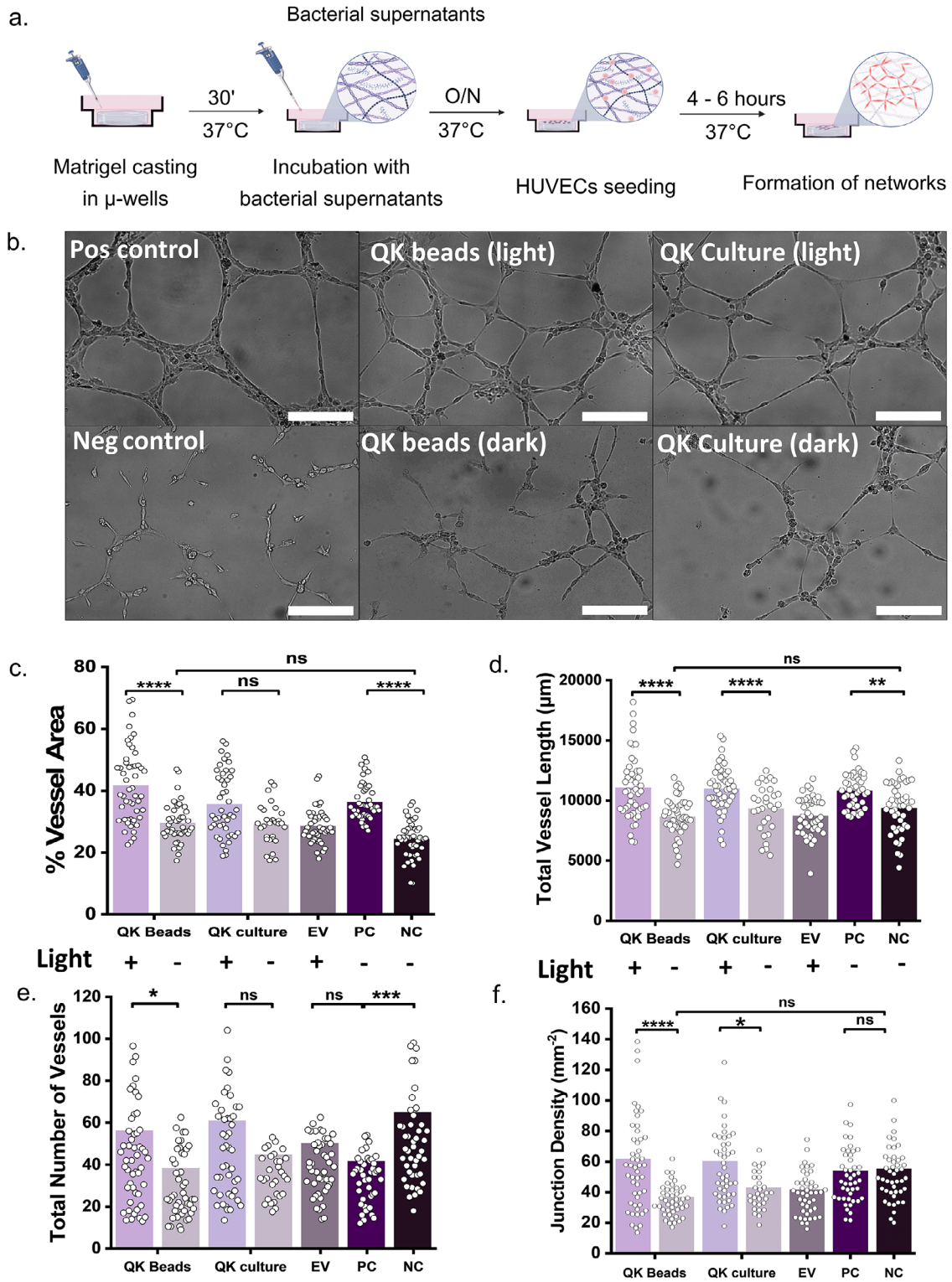

FIGURE 5 | QK-Fusion mediated HUVEC network formation from ELM and culture supernatants (a) Schematic of the Matrigel assay performed to analyze 2D HUVEC networks. Growth Factor reduced Matrigel was cast in µ-wells and polymerized for 30 mins, followed by overnight incubation of supernatants from cultures and ELMs in different conditions. The next day, HUVECs were seeded onto the Matrigel and network formation was tracked for 4–6 h. (b) Representative brightfield images showing network morphology after treatment with different supernatants. Light-induced ELM and culture supernatants promote longer, continuous network formation similar to the positive control, whereas supernatants from ELMs and culture kept in the dark form shorter and discontinuous networks like the negative control. Brightness and contrast of the images have been adjusted for maximal visualization. Scale bar denotes 200 µm (c–f) Quantitative analysis of angiogenic parameters using ImageJ and AngioTool: (c) Percentage of vessel-covered area (d) Total vessel length (µm) (e) Total number of Vessels (f) Junction Density (mm^{-2}). Bars represent mean value; dots represent each individual datapoint ($N = 3$, $n = 5$). (EV: Empty Vector, PC: positive Control, NC: Negative Control).

reflect the coverage of the network and the quality of the vessels [38].

The average percentage of area covered by vessels (vessel area) was the highest in light-induced beads. Both light-induced culture and beads were comparable to the positive control, indicating high pro-angiogenic effects (Figure 5c). Under dark conditions, both beads and culture showed an average percentage of vessel area above the negative control and empty vector, which is consistent with the low-level background activity seen in the images (Figure 5b). However, encapsulated beads showed lower background activity compared to free culture in the dark, thus showing that the encapsulation reduced unintended angiogenic activity. The average values measured for the total vessel length also reflected the improved vessel structures formed in QK beads and cultures, showing comparable values to the ones measured for the positive control (Figure 5c). In contrast, the dark conditions formed short, discontinuous vessels similar to the negative control and empty vector. This confirmed that the secreted QK-Fusion aided in the formation of the longer capillary-like structures. The total number of vessels and junction density are parameters that show interconnected structures. The images show differences in how interconnected the networks are. The positive control presents relatively few junction points, from which typically 3 to 4 vessels arise. This led to a lower count of total vessels and junction density; however, the vessel thickness is higher, which is shown in the higher values of percentage vessel area. Interestingly, both QK beads and cultures presented slightly higher junction densities. From the images, the junctions formed in QK beads and culture conditions allowed the formation of 4–6 vessel sprouts. This is noticeable in the quantification of the total number of vessels. For the control conditions (negative control, QK beads, and culture in dark), the presence of disconnected networks was reflected in the quantification of the total number of vessels (Figure 5d). However, this was not reflected in the quantification of junction density, as isolated cells were segmented as vessels by the software (Figure 5e).

Taken together, QK-Fusion secreted from the light-induced QK-beads supported levels of network formation comparable to those observed under induced culture supernatants and positive control, despite the substantially lower amount of peptide released relative to culture supernatants. This observation partially aligns with findings reported by Nakatsu et al., who demonstrated that lower concentrations of $VEGF_{165}$ promote the formation of thinner, more organized, and stable vascular structures, whereas higher concentrations lead to wider and less organized vessels [39]. In our system, the ELMs may therefore be delivering QK at concentrations that remain within an effective range for supporting vessel formation, while the higher peptide levels present in culture supernatants could potentially approach concentrations where signaling responses begin to plateau or become less efficiently translated into organized angiogenic structures.

2.6 | Chick Chorioallantoic Membrane (CAM) Assay

After the positive results obtained from the in vitro network formation assays, we moved to investigate the angiogenic potential of the ELMs in a more complex, in vivo-like environment. We selected the chick chorioallantoic membrane (CAM) assay that makes use of the highly vascularized extraembryonic chorioallantoic tissue of the developing embryo to assess new vessel formation (Figure 6a). To do this, fertilized eggs were incubated (37.5°C, 60% relative humidity, rocking) until embryonic developmental day 7 (EDD7). The viability of the embryos and the localization of the air sac were determined by candling the eggs. After locating the air sac, a window was opened right on top, carefully removing the eggshell to expose the CAM. Different conditions were investigated—QK beads (NIR induced and uninduced), empty beads, QK culture supernatants and as a negative control, untreated CAM. After placing the beads on top of the CAM (Figure 6b), the windows were closed, and the chick embryos were incubated for 7 days (EDD14). On that day, the viability of the embryo was recorded, and the CAMs were excised and fixed for further staining and analysis (Figure 6c). Embryo viability at the end of the experiment was high for NIR-induced QK beads and comparable to QK cultures and the negative control, showcasing the good biocompatibility of the system (Figure 6d; Figure S7a).

The CAMs were stained with the blood vessel marker for endothelial cells, CD34, together with actin cytoskeleton and nuclei stains (Figure 7). Several maps of the CAMs were acquired for analysis with AngioTool (ImageJ). Representative samples of the binary vessel masks and corresponding skeletonized vascular networks used for quantitative analysis are shown in Figure S7b. The percentage of area covered by blood vessels was quantified first (Figure S7c). As expected, the highest coverage was achieved by the negative control, which presents the highest number of mature, stable vessels. These vessels are typically bigger in size, covering more area in the images. This parameter is not indicative of angiogenic potential, as the newly formed capillaries are usually observed as smaller sprouts. This is why we focused our quantification on the junction density and the number of endpoints (Figure 6e,f). Of all the treated conditions, induced QK beads presented the highest junction density quantification, although not statistically different to the negative control. When looking at the number of endpoints, induced QK beads and QK cultures presented the highest numbers, strongly indicating higher numbers of newly formed capillaries.

Notably, the CAM assay is known to display biological variability between embryos, and outcomes can differ depending on the vascular parameters analyzed. Previous studies investigating photobiomodulation in the CAM model have taken strong directional increases in quantified parameters as an indication of vascularization in light-treated conditions despite a lack of statistical significance, highlighting the sensitivity of the model to biological trends [40, 41]. Apart from this, it is interesting to note that induced QK beads produced around fourfold less QK-Fusion protein than QK cultures (due to restrictive bacterial growth in the ELM and slow diffusion of QK-Fusion through the alginate bead). Thus, despite the lower production rate and possible biological variability between embryos, the light-induced QK bead CAM samples consistently yielded better outcomes on average in terms of embryo survival, number of endpoints, and junction density compared to dark-state QK beads or blank beads. Put together, these results indicate increased

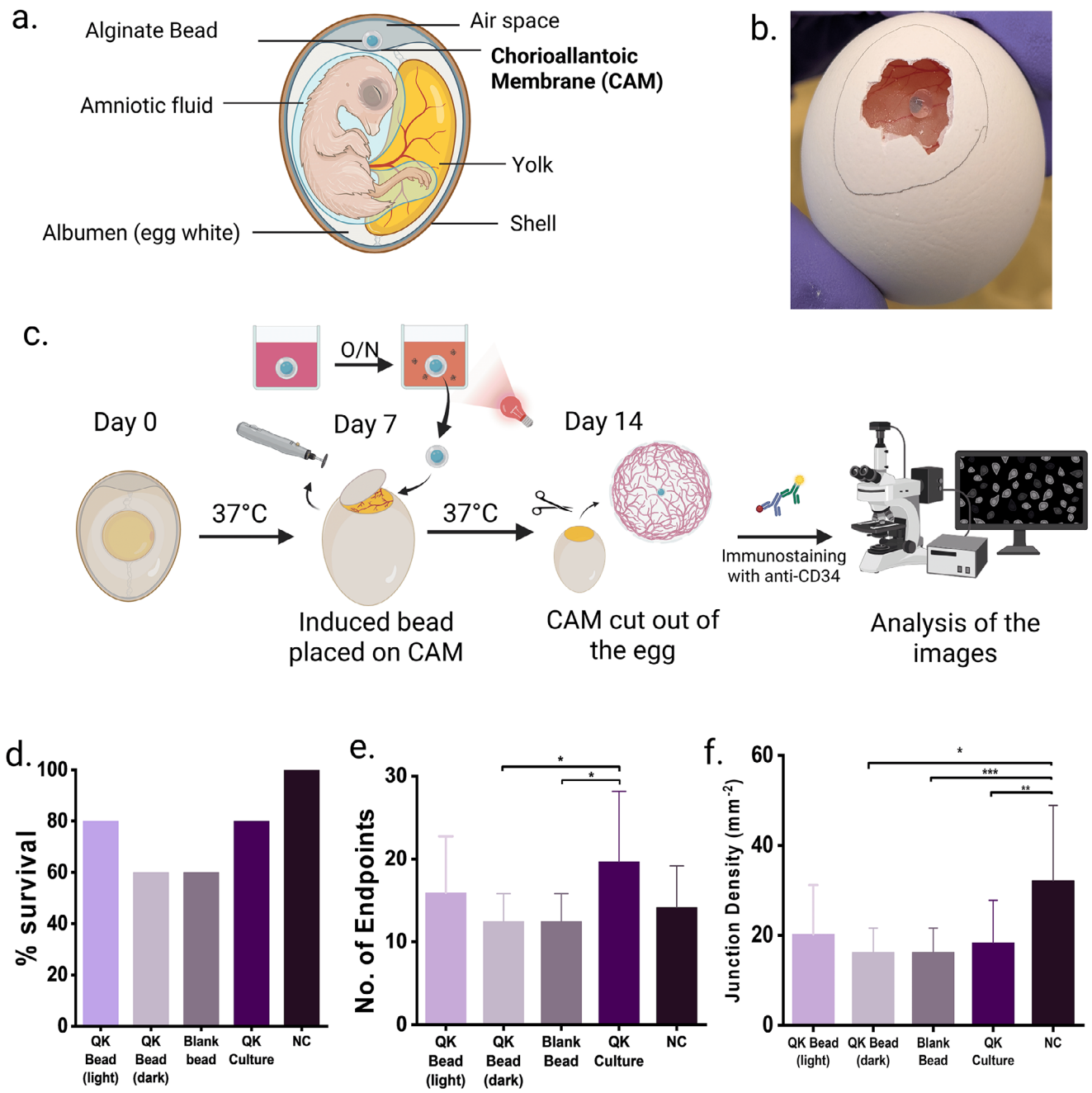

FIGURE 6 | Chick Chorioallantoic Membrane (CAM) Assay (a) Schematic representation of a chick embryo in the egg highlighting the chorioallantoic membrane (CAM) with the alginate bead. (b) Representative image of the CAM window and the implanted alginate bead on the CAM on EDD7. (c) Schematic representation of the experimental timeline: Fertilised eggs were incubated at 37.5°C designated as day 0; on EDD7, a window was opened on the eggs, and beads induced overnight were placed on the CAM. On Day 14, CAMs were excised, immunostained, and imaged. (d–f) Quantification of viability and vessel parameters across the following conditions: induced and uninduced QK-Fusion beads, induced QK-Fusion culture supernatant, bacteria-free blank beads, and untreated CAM as a negative control. (d) Endpoint embryo survival rate across various conditions ($n = 5$). (e) Quantification of the total number of endpoints. (f) Quantification of junction density (mm^{-2}). Data is presented as mean ± SD. ($N = 5$, $n \geq 10$).

angiogenic activity by the CAMs exposed to light-induced QK-beads.

Further optimization of the method could be explored in the future by using multiple beads instead of one or modifying the setup to enable NIR-induction of QK-Fusion protein production during incubation with the chick embryos. However, these may impart additional effects on embryo survival or CAM development that would need to be iteratively tested to develop the optimized method. Nevertheless, these results show the potential applicability of this ELM system in a more realistic in vivo environment.

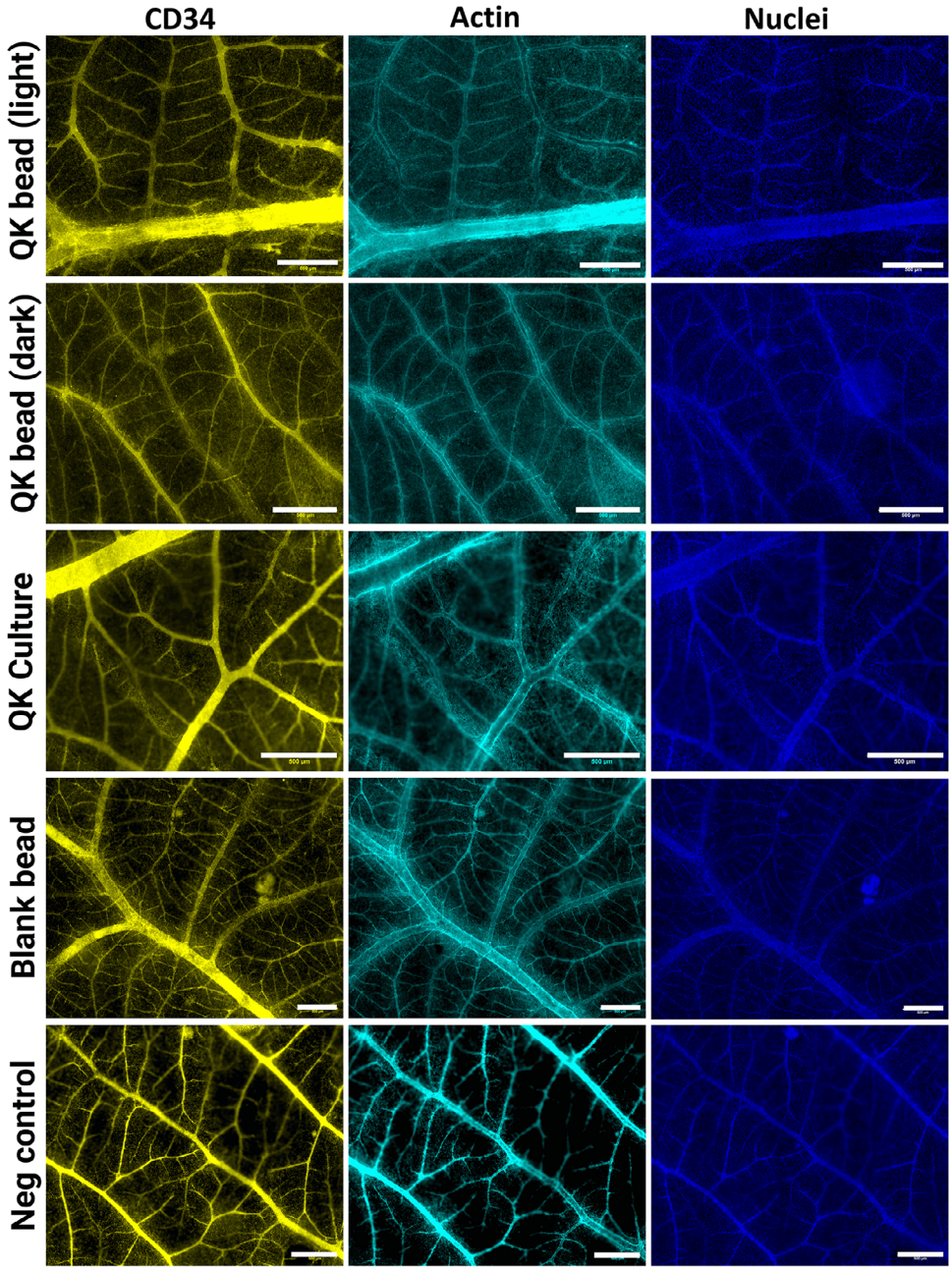

FIGURE 7 | Fluorescence microscopy images of CAMs from different treatment conditions: induced and uninduced QK-Fusion beads, induced QK-Fusion culture supernatant, bacteria-free blank beads, and untreated CAM as a negative control. The CAMs were stained with a blood vessel marker for endothelial cells, CD34 (yellow), actin cytoskeleton (cyan), and nuclei (blue). Brightness and contrast were adjusted for maximal visualisation.

3 | Discussion

Chronic and non-healing wounds remain a major therapeutic challenge due to persistent inflammation and impaired angiogenesis [42]. Near-Infrared photobiomodulation offers a non-invasive means to address these barriers by promoting tissue repair through mitochondrial activation, enhanced ATP production, and anti-inflammatory signaling [43]. However, while NIR stimulation reenergizes the wound microenvironment, it does not inherently provide targeted pro-angiogenic cues required for vascularization. Complementing NIR therapy with peptidomimetics such as VEGF-derived QK offers a rational strategy to provide stable and cost-effective alternatives to full-length growth factors for controlled vascular repair. Integrating optogenetics with engineered living materials enables simultaneous physical stimulation and dynamic therapeutic production in a single platform.

In this work, we developed an NIR-responsive ELM composed of the probiotic *E.coli* Nissle 1917, engineered with an optogenetic circuit encapsulated within alginate core–shell beads. Although direct topical use of live EcN in wound settings remains limited, previous studies demonstrate its adaptability beyond the gastrointestinal tract when appropriately engineered and

controlled [44, 45]. The core–shell architecture was selected to physically confine bacteria while permitting diffusion of secreted peptides. Supernatant plating confirmed effective short-term biocontainment, with no detectable leakage during clinically relevant timeframes. Furthermore, no significant cytotoxicity was observed when the supernatants were applied to highly sensitive HUVEC cultures.

From the materials perspective, the alginate beads demonstrate high structural integrity under physiological conditions, retaining 94% ± 2.5% of their initial wet mass over 10 days, corresponding to only ~6% mass loss. They also retained their shape and integrity during extended storage in hydrated conditions. The slight shrinkage observed upon removal from hydrated environments is consistent with reversible dehydration behavior characteristic of ionically crosslinked alginate hydrogels rather than polymer degradation [46]. These findings confirm that the encapsulation strategy provides durable structural support compatible with regenerative applications.

From a functional perspective, the optogenetic circuit allowed NIR-responsive secretion both in planktonic and encapsulated conditions. It also enabled the ELM to have reversible and intensity-dependent secretion of the VEGF-mimetic QK-Fusion protein under 800 nm illumination. While secretion gradually declined during prolonged encapsulation, recovered bacteria retained inducibility upon re-culturing, indicating preserved genetic stability. This suggests that the reduced output within the ELM state arises from microenvironmental constraints rather than circuit instability or loss of viability. This behavior is consistent with the widely reported phenomena of restricted oxygen diffusion within alginate hydrogels, which, in turn, might have directly influenced the activation of the NIR-responsive circuit [29–31]. The integrated heme oxygenase enzyme requires molecular oxygen for conversion of heme to biliverdin, the chromophore necessary for phytochrome-mediated light sensing [32]. Future studies would therefore focus on modifying the material for better gas diffusion, possibly via the addition of perfluorocarbons [47], altering the molecular network of the hydrogel with other polymers [48], or reducing the thickness of the hydrogel.

Optical activation was achieved using an 800 nm LED source at an irradiance of 0.2 mW cm^{-2}, which is substantially lower than commonly applied photobiomodulation intensities (1–50 mW cm^{-2}) and multiple orders of magnitude below maximum permissible exposure limits for skin (~200 mW cm^{-2}) [33–36]. No noticeable temperature increase was observed during illumination, confirming that the system operates well within established photobiological safety margins.

The encapsulated systems supported the formation of elongated, organized, and interconnected HUVEC networks comparable to those generated by culture-based systems, despite secreting lower overall amounts of peptide. This observation suggests that the spatial and temporal presentation of angiogenic cues may play an important role in regulating vascular morphogenesis. Previous studies have shown that sustained or unregulated VEGF exposure can induce aberrant vascular growth, whereas more controlled signaling promotes the formation of organized and functional microvasculature [39, 49, 50]. While basal secretion was statistically indistinguishable from the negative control in vitro, further monitoring of dark-state expression and reduction will be considered in future in vivo studies where sensitivity to angiogenic cues may be higher.

The angiogenic potential of our system was further studied in line with the 3Rs (Replacement, Reduction, Refinement), in an in vivo-like environment using the well-established chick chorioallantoic membrane (CAM) assay [51, 52]. Induced QK-Fusion secreting beads triggered localized vascular capillary formation confirming that the secreted peptide remains active in a tissue-like environment. While not all quantitative parameters reached statistical significance, the induced condition consistently showed higher junction density and endpoint numbers across independent embryos, supporting a reproducible pro-angiogenic effect. Variability between embryos is inherent to the CAM assay, and similar directional increases in vascularization have been reported in photobiomodulation studies using this model [40, 41].

Future studies could directly compare the same total dose delivered continuously versus in defined, programmed activation intervals to better understand the benefits of dynamic release. Such experiments would first require establishing the appropriate therapeutic dose and delivery window for this ELM in an in vivo wound model. Evaluation in mammalian wound models will therefore be an important next step to assess therapeutic efficacy, tissue remodeling, and host immune responses under clinically relevant conditions.

Together, these findings establish a framework for externally programmable ELMs that integrate optical control with spatially confined therapeutic delivery for regenerative medicine applications.

4 | Conclusion

In this work, we developed an NIR-responsive ELM that integrates optogenetic control with alginate-based core–shell encapsulation of *E. coli* Nissle 1917 to enable programmable secretion of a VEGF-mimetic QK-Fusion peptide. The material architecture provided effective bacterial confinement while maintaining structural stability and peptide diffusion under physiological conditions. NIR illumination enabled reversible and intensity-dependent secretion, allowing external regulation of therapeutic output. The secreted peptide promoted endothelial network formation in vitro and induced localized vascularization in the CAM assay, demonstrating biological functionality in a tissue-like environment. Together, these findings establish a platform for spatially controlled delivery of pro-angiogenic cues using optically programmable living materials. Future studies in mammalian wound models will further evaluate therapeutic efficacy, immune interactions, and translational potential for regenerative medicine applications.

5 | Materials and Methods

5.1 | Bacterial Strain, Media, and Plasmids

5.1.1 | AvNIRusk- QK-Fusion Plasmid Creation

The QK-Fusion construct was ordered as an eBlock from Integrated DNA Technologies (IDT) and codon-optimized using the IDT codon Optimization Tool. The gene was cloned into the *Av*NIRusk plasmid (pMH028, [22]) replacing the *Ds*Red reporter gene using NEBuilder HiFi Assembly cloning kit (New England Biolabs GmbH, Germany, E5520S). For creation of the empty vector (EV) control, the *Av*NIRusk plasmid was amplified excluding the *Ds*Red gene, and circularized using the KLD Enzyme Mix (New England Biolabs GmbH, Germany, E0554S). The gene sequences and primers are listed in Table S1. All plasmids were initially transformed into NEB 5-alpha Competent *E. coli* cells (New England Biolabs GmbH, Germany, Art. No. C2987) and plated on LB agar supplemented with 50 µg/mL kanamycin ((kanamycinsulfat, Carl Roth GmbH, Germany)). Positive clones were screened by colony PCR, followed by plasmid extraction (ThermoFisher Scientific, K210011) and Sanger sequencing (Eurofins Genomics) to verify the sequence of the construct.

5.1.2 | Preparation of Chemically Competent *E. coli* Nissle 1917

An overnight culture of wild-type *E. coli* Nissle 1917 grown at 37°C, 250 rpm was subcultured into 50 mL of fresh LB to a starting OD_{600} of 0.01. The culture was grown under the same conditions until log phase ($OD_{600} \approx 0.3–0.4$). The cells were then chilled on ice and pelleted by centrifugation at 4000 rpm for 10 min at 4°C. To prepare the cells for transformation, the pellet was washed twice with 10 mL of freshly prepared, ice-cold 200 mM calcium chloride solution (Carl Roth GmbH, Germany), followed by a single wash with 10 mL of a 1:1 mixture of 200 mM $CaCl_2$ and 10% (w/v) glycerol. After the final wash, the pellet was gently resuspended in 1 mL of the same $CaCl_2$:glycerol mixture. Aliquots of 50 µL were prepared and either used immediately or stored at –80°C for future transformations.

5.1.3 | Transformation Into *E. coli* Nissle 1917

Sequence-verified *Av*NIRusk-QK-Fusion plasmid and empty vector plasmids were transformed into EcN via heat-shock. Briefly, about 500 ng of plasmid DNA was gently mixed with 50 µL of chemically competent *E. coli* Nissle 1917 cells and incubated on ice for 30 min. The mixture was then subjected to a heat-shock at 42°C for 30 s using a water bath, followed by immediate cooling on ice for 5 min. Nine hundred microliters of pre-warmed SOC medium was added to the cells, and the suspension was incubated at 37°C for 1 h with shaking to allow recovery. After recovery, 200 µL was spread onto LB agar plates containing 50 µg/mL kanamycin, and the plates were incubated at 37°C overnight. All procedures were performed under dark or low-light conditions to avoid unintended activation.

5.2 | Bacterial Performance Testing

5.2.1 | Bacterial Culture for Secretion

EcN carrying the desired plasmid was grown from cryoculture stocks in Luria–Bertani (LB) medium supplemented with kanamycin (50 µg mL^{-1}) at 37°C with shaking at 250 rpm for 16 h. The overnight culture was diluted to an initial OD_{600} of 0.01 into fresh LB medium with kanamycin under two conditions: induced and uninduced. Cultures were incubated at 37°C until mid-log phase ($OD_{600} = 0.6–0.8$), followed by centrifugation at 4000 rpm for 10 min at room temperature. The resulting cell pellets were either resuspended in LB medium or Medium 199 (M199; Gibco) containing kanamycin (50 µg mL^{-1}).

NIR illumination was performed using a custom-built LED setup consisting of six 800 nm LED bulbs (LED800-01AU, Roithner Lasertechnik) arranged in a 3 × 2 matrix on a flat base. The base was fitted with a holder accommodating six 10 mL culture tubes positioned at a 30° tilt, maximizing bacterial growth. The LEDs were connected to a control unit containing a master switch and three independent channels, each governing a pair of bulbs. Each channel was equipped with an individual on/off switch and a potentiometer allowing fine-tuning of light intensity across 10 major divisions, with 100 incremental steps per division. The system was calibrated using a power meter to deliver a light intensity of 2 mW cm^{-2} at the sample plane during induction experiments.

For induction, cultures were exposed to near-infrared (NIR) light at 800 nm with an intensity of 2 mW cm^{-2} for 20–22 h at 37°C. Uninduced samples were protected from light using aluminum foil.

5.2.2 | Fluorescence Validation of Supernatants on DNase Agar Plates

To validate fluorescence of secreted proteins and visually confirm that *Ds*Red expression does not induce DNA degradation, a DNase agar plate supplemented with kanamycin (50 µg/mL) was divided into three zones. Onto each zone, 5 µL of mid-log phase bacterial cultures were spotted: (i) *E. coli* Nissle 1917 expressing QK-Fusion, (ii) EcN expressing *Ds*Red, and (iii) an empty vector (EV) control. The plate was incubated under NIR light to induce expression and imaged after 16–18 h using a ChemiDoc MP imaging system.

5.2.3 | Fluorescence Quantification

E. coli Nissle 1917 carrying the *Av*NIRusk–*Ds*Red construct was first grown overnight in LB medium at 37°C with shaking (250 rpm). The next day, cultures were diluted to $OD_{600} \approx 0.01$ in fresh LB medium supplemented with kanamycin and incubated until mid-log phase ($OD_{600} = 0.4–0.6$). The cultures were pelleted down (4000 rpm, 10 mins) and resuspended in the same volume M199 medium supplemented with kanamycin. Cultures were then exposed to 800 nm NIR light or kept in the dark overnight at

37°C. The following day, 500 µL from each culture was harvested, pelleted (4000 rpm, 5 min), and resuspended in PBS to a final OD_{600} of 1. A volume of 200 µL of each normalized suspension was transferred into black, clear-bottom 96-well plates (Greiner Bio-One, Germany). Fluorescence was measured on a TECAN microplate reader (Infinite 200 Pro, Tecan Deutschland GmbH, Germany) using excitation at 500 ± 9 nm, emission at 554 ± 9 nm. Fluorescence values were normalized to OD_{600} to account for cell density differences.

5.2.4 | Light-Dose-Response Assay

To assess the NIR light-induced expression of the fluorescent reporter *Ds*Red in *E. coli* Nissle 1917, light-dose responses were recorded as before [22]. In brief, bacteria containing *Av*NIRusk-*Ds*Red or an empty vector control were grown in 5 mL LB medium supplemented with 50 µg mL^{-1} kanamycin (LB-Kan) at 30°C and 225 rpm agitation for 21–24 h in darkness (non-inducing conditions). All subsequent steps were performed under green safe light. The 100-fold diluted bacteria were distributed in 200 µL per well in a black-walled microtiter plate with clear bottom (µClear, Greiner BioOne, Frickenhausen, Germany). Different NIR light intensities were applied using a custom-made 8-by-8 LED matrix reported in ref. [53] emitting at (800 ± 18) nm controlled by an Arduino circuit board. The light intensities were calibrated with a power meter (model 842-PE, equipped with a 918D-UV-OD3 silicon photodiode, Newport, Darmstadt, Germany). After an 18 h incubation at 37°C and 750 rpm agitation, the OD_{600} and *Ds*Red fluorescence with excitation and emission wavelengths of (500 ± 9) nm and (554 ± 9) nm were recorded with a Tecan Infinite M200 Pro MTP reader (Tecan Group, Ltd., Männedorf, Switzerland). The *Ds*Red fluorescence was normalized by OD_{600}, and the empty vector background was substracted. Data are represented as a function of the light intensity averaged over the duty cycle and are described by Hill isotherms using the Fit-o-mat software [54, 55].

5.2.5 | Nuclease A Secretion Assay on Agar Plates

The Difco DNase test agar (Fisher Scientific) was prepared according to the manufacturer's instructions and 0.05 g L^{-1} of the methyl green indicator (Serva) was added manually. A bacterial colony containing the *Av*NIRusk-NucA was resuspended in 20 µL phosphate-buffered saline, and 1 µL was dropped per agar plate. The plates were incubated at 37°C overnight in darkness or under constant NIR light applied with the Arduino-controlled custom-built LED matrix.

5.2.6 | Nuclease A Assay With Supernatants

DNase media was prepared by precipitating agar from the commercial DNase Agar (Altmann Analytik GmbH, Germany), followed by sterilization by autoclaving. The final formulation comprised of Tryptose (20 g/L), Sodium Chloride (5 g L^{-1}), Calf Thymus DNA (2 g L^{-1}), and Methyl Green (0.05 g L^{-1}). For measuring secretion from bacterial cultures, the supernatants from the uninduced and induced cultures were filter-sterilized using 0.22 µm syringe filters. They were then mixed with DNase media in a 1:1 ratio for a final volume of 800 µL. Following preparation, tubes were wrapped in aluminum foil to prevent light-induced degradation of methyl green. All samples were incubated at 37°C with shaking at 250 rpm for 4 h. After incubation, 200 µL from each dilution was transferred in triplicate to a black 96-well plate with a transparent bottom. Fluorescence was measured using a Microplate Reader (Infinite 200 Pro, Tecan Deutschland GmbH, Germany) at an excitation/emission wavelength of 633/668 nm, with the Z-position set at 19 000 µm and gain at 100.

5.2.7 | Standard Curve Preparation

For the standard curve preparation, DNase media was added to the cell-free supernatant of *E. coli* Nissle 1917 harboring the Empty Vector, collected after 16 h of NIR light induction, in a 1:1 ratio. Using this solvent as a base, serial dilutions of pure NucleaseA protein (Sigma-Aldrich) were prepared in 1.5 mL Eppendorf tubes for concentrations of 200, 100, 50, 25, 12.5, 6.25, 3.12, and 1.56 nM, for a final volume of 800 µL. After incubation, 200 µL from each dilution was transferred in triplicate to a black 96-well plate with a transparent bottom. Fluorescence was measured using a Microplate Reader (Infinite 200 Pro, Tecan Deutschland GmbH, Germany) at an excitation/emission wavelength of 633/668 nm, with the Z-position set at 19 000 µm and gain at 100.

5.2.8 | Matrigel Preparation

Growth factor reduced (GFR) Matrigel (356 231, Corning) aliquots were thawed overnight at 4°C. A box of 10 µL filter tips was also pre-chilled at 4°C to prevent premature polymerization during handling. The following day, 10 µL of cold Matrigel solution was carefully dispensed into each well of a pre-chilled 96-well 3D µ-Plate (Ibidi) on ice. The plate was then incubated at 37°C for 30–45 min to allow complete gelation.

5.2.9 | Collagen Binding Assay

Supernatants from overnight induced and uninduced bacterial cultures were collected by centrifugation at 4000 rpm for 10 mins. Fifty microliters of these supernatants were then pipetted in each well and the plate was incubated in the dark at 37°C for 90 min. After incubation, each of the wells was washed thrice with sterile PBS. Each wash was performed very carefully to not disrupt the Matrigel surface. Matrigel-bound QK-Fusion was quantified by Split-Luciferase Assay. Empty vector culture supernatant was used as a negative control.

5.2.10 | Split-Luciferase Assay

Split-luciferase experiments were performed in white, 96-well flat-bottomed microplates and measured using a microplate reader (Infinite 200 Pro, Tecan Deutschland GmbH, Germany). The measurements were performed in triplicate with an integration time of 1000 ms for each measurement. LgBiT protein was always freshly thawed and diluted to 1 µM in PBS. The

substrate solution was prepared by diluting Furimazine (Nano-Glo Luciferase Assay Substrate, Promega) in Nano-Glo Luciferase Assay Buffer in a 1:50 ratio. The substrate solution was always freshly prepared, protected from light, and directly added prior to the measurements. In the well plates, 12.5 µL of LgBiT was added to 12.5 µL of each sample supernatant. Consequently, to each of the wells, 25 µL of the substrate solution was added, and the luminescence measurements were performed in the plate reader after incubating the plate in the dark for 10 min. The plate was also imaged in the ChemiDoc MP imaging system on the chemiluminescence channel. Empty vector supernatants were used as a negative control.

5.3 | Fabrication and Characterization of ELMs

5.3.1 | Bacterial Culture for ELMs

Escherichia coli Nissle 1917 (EcN) carrying the desired plasmid was grown from glycerol stocks in Luria–Bertani (LB) medium supplemented with kanamycin (50 µg mL^{-1}) at 22°C with shaking at 250 rpm for 16 h.

5.3.2 | Fabrication of ELMs

Sodium alginate medium viscosity, sodium alginate from brown algae, Sigma-Aldrich, Cat. No. 71238, Merck Life Science, Germany; estimated molecular weight ≈120–190 kDa) was used as the polymer for the ELMs. The core–shell alginate beads were fabricated following the protocol described in [21] with certain modifications for encapsulating *E. coli* Nissle 1917. Briefly, *E. coli* Nissle 1917 cultures were grown to mid-log phase (OD_{600} = 0.3–0.5), harvested by centrifugation at 4000 rpm for 10 min, and resuspended in Medium 199 (M199, Gibco) containing 50 µg mL^{-1} kanamycin and 0.4 w/v% glucose. The bacterial suspension was mixed with 3 wt.% alginate (Sigma-Aldrich in a 1:2 volume ratio to form a 2 wt.% alginate–bacteria mixture, supplemented with 1% v/v Alcian blue for visual tracking. Droplets (10 µL) were dispensed into a 6 wt.% $CaCl_2$ solution and allowed to crosslink for 30–45 min, forming the alginate core beads.

To generate the shell layer, a 1.5 wt.% alginate shell solution was prepared by diluting the 3 wt.% alginate stock 1:1 with Milli-Q water and vortexed for uniformity. Each previously formed alginate core bead was dipped into the shell solution and transferred—along with approximately 25 µL of shell solution—into an 8 wt.% $CaCl_2$ crosslinking bath using a modified pipette tip (tip cut to widen the bore). The core–shell beads were allowed to solidify in $CaCl_2$ for 4–5 h at room temperature to ensure complete ionic crosslinking. Finally, beads were washed with sterile Milli-Q water and transferred into a 96-well plate with 250 µL of M199 media + kanamycin in each well. The plate was covered in aluminum foil and left overnight in a 37°C incubator for the bacteria to grow.

5.3.3 | Bacterial Leakage

Potential bacterial leakage from the beads was monitored by directly spotting 5 µL of the supernatant from the bead-containing wells on to LB agar plates supplemented with Kanamycin (50 µg mL^{-1}). Plates were incubated overnight at 37°C and inspected for bacterial colony formation. Figure S5a shows a representative image of an agar plate on day 10 of bead fabrication.

5.3.4 | Bead Mass Stability Assessment

The structural stability of the alginate beads under physiological conditions (37°C, pH ∼ 7.4) was assessed using blank (bacteria-free) core–shell beads, incubated in M199 medium for 10 days. The beads were carefully removed, blotted with lint-free tissue to remove excess surface liquid, and weighed using an analytical balance. After weighing, the same beads were returned to the medium and incubated further under identical conditions. The medium was replenished every 2–3 days to compensate for evaporation. The percentage change in mass relative to the initial weight was calculated and plotted to monitor mass loss over time (Figure Sx). The data represent measurements from three independent batches with three beads per batch.

5.3.5 | Switchable Secretion

Core–shell alginate beads containing *E. coli* Nissle 1917 engineered for NIR light-responsive QK-Fusion expression were incubated overnight at 30°C in M199 medium supplemented with 50 µg mL^{-1} kanamycin. Blank beads devoid of any bacteria and beads with an empty vector containing *E. coli* Nissle 1917 were used as controls. The following day, beads were distributed into three sterile 96-well plates to test different illumination conditions: one plate was kept under 800 nm NIR light (0.2 mW cm^{-2}), one plate was maintained in complete darkness (wrapped in aluminium foil) and a third plate was subjected to alternate light and dark cycles, with illumination switched every 24 h. All plates were incubated at 30°C. For the plates kept under NIR-illumination, the light source was turned off 2 h prior to supernatant collection to allow diffusion of the secreted peptide form the hydrogel into the surrounding medium. Every 24 h, 25 µL of supernatant was collected from each well for analysis, and the medium was completely replaced with fresh supplemented M199. In the alternating condition, the illumination state was reversed at each 24 h interval, while the constant light and constant dark plates remained under their respective conditions throughout the experiment. This switching cycle was continued for six consecutive days. The peptide detection was done with the help of the Split nanoluciferase assay by adding 25 µL of LgBiT and 50 µL of diluted substrate to the 25 µL of supernatant and measuring luminescence signals in the plate reader after 10 min of incubation in the dark.

5.3.6 | Light Dose-Response Assay With ELM Supernatants

To characterize the dose-responsive behavior of our NIR-controlled system, we measured QK secretion under a gradient of light intensities (0, 10, 20, 40, 60, 80, 100, 150, and 250 µW cm^{-2}), analogous to the approach described earlier. Fresh beads were allowed to grow for two days at 30°C. They were then induced

under each defined intensity for 24 h using a custom-made 8-by-8 LED matrix [53] emitting at (800 ± 18) nm controlled by an Arduino circuit board. Following induction, supernatants were collected, and 25 µL of each was assayed by split-luciferase to quantify secreted QK-Fusion. The resulting intensity–response data were fitted in Origin v9.9 using a Hill model ($y = V_{max}x^n/(k^n + x^n)$), yielding $RLU_{max} = 5.2 \times 10^5$, $I_{50} = 98.5\ \mu W\,cm^{-2}$, where I_{50} refers to the light dose required for half-maximal activation, $n = 9.98$, and $R^2 = 0.93$, confirming the tunable, sigmoidal activation of secretion with increasing NIR intensity.

5.3.7 | Bacterial Recovery From Beads

To quantify the viable bacterial population within the beads after 7, 14, and 21 days, individual beads were dissolved in 100 mM sodium citrate. Briefly, one bead was transferred to a 1.5 mL Eppendorf tube containing 500 µL of 100 mM sterile sodium citrate solution and incubated at 30°C with shaking (1000 rpm) for 10 mins. The resulting suspension was then centrifuged (4000 rpm, 4 mins), the supernatant discarded, and the bacterial pellet was resuspended in 200 µL of M199 media and serially diluted in sterile PBS up to 10^{-5}. From the appropriate dilutions, 100 µL was then plated onto LB-agar plates containing Kanamycin (50 µg/mL) and incubated at 37°C overnight. Plates were imaged using a ChemiDoc MP imaging system, and colonies were quantified using ImageJ. For automated colony counting, plate images were converted to 8-bit format, background was reduced using threshold adjustment to selectively identify colonies while excluding the plate rim, and colony numbers were quantified using the *Analyze Particles* function. Colony-forming units (CFU) were calculated as CFU per bead based on the dilution factors and plated volume. Colonies from each plate were grown in liquid culture overnight, induced for 4 h, and peptide secretion was measured with the Split-Luciferase Assay. Bacteria inoculated from cryostock, induced and uninduced, were used as controls.

5.4 | HUVECs Culture and Network Formation

5.4.1 | HUVECs Culture Conditions

Human umbilical vein endothelial cells (pooled donors, HUVECs; Lonza) were cultured on gelatin-coated flasks (0.2% w/V) to enhance adherence. Cells were maintained in Medium 199 supplemented with 20% fetal bovine serum (heat-inactivated FBS gold; PAN-Biotech, Germany), 1% penicillin-streptomycin (Sigma), 12 µg/mL endothelial cell growth supplement (ECGS; Sigma, C-30160), and 0.1 mg/mL sodium heparin (Sigma, H-3149).

5.4.2 | HUVECs Passaging and Seeding

For routine passaging, spent media was discarded from the culture flask and washed thoroughly with sterile PBS solution. For detachment of cells, approximately 2 mL/10 cm^2 pre-warmed trypsin was added to the flask and incubated at 37°C for 1–2 min till 90% of the cells were visibly detached. To stop enzymatic activity, pre-warmed complete growth medium was added at twice the volume of trypsin used. The cells were then collected in a sterile falcon and centrifuged at 1000 rpm for 7 min. After centrifugation, the supernatant was discarded, and the cell pellet was resuspended in 1 mL of complete growth medium. For counting cells, 25 µL of the cell suspension was mixed with 25 µL of Trypan Blue dye (Thermofisher). Ten microliters of this mixture was then loaded onto the cell counter (CellDrop) for counting cell number and cell viability. If the cell viability was >75%, the cells were seeded at a density of 1000 cells per cm^2 in complete growth medium in flasks lined with 0.2% w/v of gelatin. Cells were then incubated at 37°C in a humidified atmosphere containing 5% CO_2, and medium was changed every 48 h or as required.

5.4.3 | Cytocompatibility Assays

To prepare for evaluating cytocompatibility, HUVECs (10 000 cells/well) were seeded in a sterile 96-well plate (CellStar, Greiner Bio-One GmbH, Germany) in 150 µL growth media and allowed to attach and form a monolayer (37°C, 20 h, 5% CO_2). The spent media was then removed and treated with bacterial supernatants from different conditions (light-treated bacterial culture, light-treated beads, and empty vector beads). The cells were incubated for either 24 or 72 h at 37°C and 5% CO_2.

5.4.4 | Cytotoxicity Assay

Cytotoxicity was assessed via a lactate dehydrogenase assay (LDH) using the CytoTox 96 non-radioactive cytotoxicity assay (Promega). according to the manufacturer's protocol. In brief, 30 µL of supernatant from each experimental well was transferred to a fresh 96-well plate and mixed with an equal volume (30 µL) of LDH substrate solution. The reaction was allowed to proceed for 20 min at room temperature in the dark, after which 30 µL of stop solution was added to terminate the reaction. Absorbance was measured at 490 nm using a TECAN Spark microplate reader. Cells cultured in standard growth medium served as the negative control, while cells lysed with 37.5% Triton X-100 were used as the positive control. Media-only wells were included to correct for background absorbance, termed as 'blank'. These blank values were subtracted from all the sample and control values. The percentage of cell death was then calculated as:

$$\left(\frac{Sample}{Lysis\ Control}\right) \times 100$$

5.4.5 | Cell-Viability Assay

Cell viability was assessed using the AlamarBlue reagent (Invitrogen) according to the manufacturer's instructions. In brief, a 10% (v/v) solution of AlamarBlue in growth medium was added to cells treated with the supernatants. Cells maintained in standard growth medium served as positive control, while medium-only wells were included as blanks. Fluorescence (Ex/Em 570/600 nm) values were recorded using a TECAN Spark microplate reader. Blank values were subtracted from all the sample and control values.

5.4.6 | Live/Dead Staining

To further evaluate cytocompatibility, Live/Dead staining was performed after 24 and 72 h incubation with bacterial supernatants using the LIVE/DEAD BacLight Bacterial Viability Kit (Thermo Scientific, L7012). Following the AlamarBlue assay, HUVECs were gently washed thrice with PBS and incubated with a staining solution prepared by adding 1.5 µL SYTO9 and 1.5 µL Propidium Iodide (PI) to 1 mL of 1% BSA solution. Cells were incubated with 100 µL of the staining mixture for 20 mins at room temperature in the dark. Fluorescence imaging was performed using an inverted epifluorescence microscope (Leica DMI6000 B) at 10× magnification. Live cells were identified by green fluorescence (SYTO9), while membrane-compromised or dead cells exhibited red fluorescence (PI). Cells treated with 100 µL of 70% ethanol for 20 mins were used as a positive control for membrane damage. Representative images were recorded for qualitative assessment of cell viability.

5.4.7 | Network Formation Assay

For the endothelial network formation assay, growth factor-reduced Matrigel (Corning) was thawed overnight at 4°C. A volume of 10 µL of Matrigel was dispensed into each well of angiogenesis assay plates on ice and incubated at 37°C for 30–45 min to allow polymerization. Following gelation, 50 µL of treatment solution was added to each well in triplicate and incubated overnight at 37°C. HUVECs at 60%–70% confluency were cultured in Medium 199 (M199) supplemented with 5% fetal bovine serum (FBS) and 1% penicillin-streptomycin (P/S) for 20 h. After this conditioning period, cells were harvested by trypsinization and were neutralized using pre-warmed complete medium. Cells were pelleted by centrifugation and resuspended in M199 supplemented with 1% P/S. The suspension was adjusted to a final density of 15 000 cells in 50 µL. Prior to cell seeding, the treatment-containing medium was removed from the Matrigel-coated wells. The cell suspension (50 µL) was gently added to each well and allowed to attach for 1 h at 37°C. Plates were then incubated at 37°C in a humidified 5% CO_2 incubator for 6 h, and network formation was monitored hourly using bright-field microscopy.

5.4.8 | Image Acquisition for Time-Lapse Imaging

To monitor HUVEC network formation in real time, live-cell imaging was conducted using an Observer Z1 inverted wide-field microscope (Carl Zeiss, Oberkochen, Germany), equipped with a temperature-controlled incubation unit maintained at 37°C and a 5% CO_2 atmosphere. The µ-slides were prepared as previously described and immediately transferred to the microscope's incubation chamber. Phase-contrast images were captured using a Zeiss EC Plan-Neofluar 10×/0.3 Ph1 objective lens, without additional magnification, at 20-minute intervals over 22 h. Image acquisition was performed using a Prime BSI Express sCMOS camera (Teledyne Photometrics, USA), with ZEN software (version 3.5, ZEISS) controlling the imaging process. For each experimental condition, three non-overlapping fields per well were imaged, with a minimum of two biological replicates.

5.4.9 | Image Acquisition for Endpoint Microscopy

Brightfield images from the Matrigel-based network formation assay were acquired using a Leica DMI6000 B epifluorescence microscope at 10× magnification after 4hours. Five non-overlapping fields were imaged per well, with at least three biological replicates per condition. The experiment was independently repeated three times across all seven experimental groups.

5.4.10 | Image Analysis

Brightfield images from the Matrigel-based angiogenesis assay were acquired using a Leica DMI6000 B epifluorescence microscope at 10× magnification. Five non-overlapping fields were imaged per well, with at least three biological replicates per condition. The experiment was independently repeated three times across all seven experimental groups. Image analysis was performed in Fiji (ImageJ) 2.16/1.54 p using the trainable Weka segmentation (TWS) plugin and the AngioTool plugin. The AngioTool plugin extracted the following parameters: vessel area, total vessel length, junction density, and number of endpoints and junctions. Vessel area was calculated as the fraction of the image occupied by vessel-like structures. Total vessel length was calculated as the sum of all detected vessel segment lengths, junction density was calculated as the number of branching points per unit image area, and the number of endpoints was calculated as per Equation (1). A custom-written macro (provided in the Supporting Information) enabled batch processing: it applied a pre-trained Weka model for vessel segmentation, thresholded the images, and generated binary masks for downstream analysis.

$$number\ of\ vessels = \left(\frac{number\ of\ junctions}{2}\right) + number\ of\ endpoints \quad (1)$$

5.5 | Chick ChorioAllantoic Membrane (CAM) Assay

5.5.1 | Incubation of Eggs

For performing the CAM assay, white specific pathogen-free research eggs (Valo BioMedia GmbH, Germany) were obtained and incubated at 37.5°C with 60% relative humidity under continuous rocking conditions until embryonic developmental day 7 (EDD7).

5.5.2 | Candling and Treatment of Eggs

On EDD7, eggs were candled to confirm viability and locate the air sac. A small window was carefully opened in the air cavity to expose the CAM under sterile conditions. The following

treatment groups were investigated: NIR-induced QK-Fusion beads, uninduced QK-Fusion beads, bacteria-free blank beads, induced QK-Fusion bacterial culture supernatants as a positive control, and untreated CAM as a negative control. Each condition had five viable eggs. Depending on the treatment group, either a single bead supplemented with 25 µL of bead supernatant or 50 µL of supernatant (positive control) or PBS (untreated CAM) was gently applied on the CAM surface. The shell window was then sealed tightly with parafilm. Eggs were returned to the incubator and maintained until Embryonic developmental day 14 (EDD14).

5.5.3 | Immunostaining of CAM

At EDD14, embryo viability was recorded prior to sample collection. CAM tissues surrounding the treatment region were excised and fixed in 4% paraformaldehyde prepared in phosphate-buffered saline (PBS) for 20 mins at room temperature with slight shaking, followed by two washes with PBS. Fixed samples were permeabilized using 0.1% Triton X-100 in PBS for 15 mins at room temperature and then washed twice with PBS. To minimize non-specific antibody binding, samples were blocked using a blocking buffer consisting of 1% w/v bovine serum albumin (BSA) in PBS for 30mins at room temperature. Following blocking, CAM tissues were then incubated overnight at 4°C with a Mouse anti-chicken CD34 primary antibody (dilution 1:200, AV138, Bio-Rad, Germany). The following day, samples were washed twice with PBS supplemented with 0.5% Tween20 (PBS-T) and incubated with donkey anti-mouse Alexa Fluor 546 secondary antibody (dilution 1:400, Invitrogen, Germany) diluted in blocking buffer for 1 h at room temperature protected from light. For visualization of cellular architecture, samples were simultaneously stained with Phalloidin (dilution 1:300, Chromotek, Germany) to label the actin cytoskeleton and 4′, 6-diamidino-2-phenylindole (DAPI) (dilution 1:1000, Invitrogen, Germany) for nuclear staining for 1 h at room temperature in the dark. After staining, CAM tissues were washed five times with PBS-T to remove excess dye and unbound antibodies. Samples were maintained in PBS during imaging. Fluorescence imaging was done using an inverted epifluorescence microscope (Leica DMI6000 B) using appropriate filter sets.

5.5.4 | Image Analysis

For quantitative image analysis, multiple regions were imaged from each CAM sample. Blood vessels including the newly formed capillaries were manually segmented and converted into binary format using ImageJ/Fiji. The images were then for quantified with the Angiotool plugin in ImageJ/Fiji. For images exceeding the size limitations of Angiotool, datasets were split into smaller tiles (2000 × 2000 pixels) prior to analysis. Partial edge tiles were excluded to ensure consistent quantification. All the images were normalized with the total image area; the tiled images were normalized as (2000 × 2000) multiplied by the number of tiles generated. The parameters quantified were the percentage of area covered by vessels, junction density, and total number of endpoints. All the parameters were normalized with the total image area for the whole images and (2000 × 2000) multiplied by the number of tiles generated for the tiled images. The scale used to convert pixels to mm was 1562.5 pixels/mm.

5.6 | Statistical Analysis

Statistical analysis was carried out using GraphPad Prism v9 software and plotted using Origin 2022 v9.9 software. All experiments were carried out in triplicate unless otherwise noted. Samples were assayed in triplicates unless otherwise noted. All graphs represent mean ± standard deviation (SD) unless otherwise noted. Students' *t*-tests were used to determine significant differences between the means of the groups. For the network formation analyses, the goodness of fit of the data was tested via Shapiro–Wilk normality test. When comparing three or more groups: normally distributed populations were analyzed via analysis of variance test (ANOVA test) performing a Tukey's post hoc test to correct for multiple comparisons; when populations were not normally distributed, a Kruskal–Wallis test was used with a Dunn's post hoc test to correct for multiple comparisons.

Differences among groups are indicated as: p-values < 0.05 (*), p-values < 0.01 (**), p-values < 0.005 (***), p-values < 0.001 (****), and differences among groups not statistically significant (ns).

Acknowledgements

We thank Prof. Wilfried Weber for generously providing the genetic parts encoding LgBiT and SmBiT, and Dr. Cao Nguyen Duong for assistance with the time-lapse microscopy experiments. We are grateful to Christian Ersfeld for constructing the custom NIR-LED device with culture tube holder used in this study and to Bruno Schäfer for helping to determine its illumination intensity with a power meter. We also acknowledge Varun Sai Tadimarri and Florian Riedel for demonstrating the bead fabrication process, Zirui Ye for assisting with the initial optimization experiments, and Ketaki Deshpande for providing the HUVEC cells. The schematic illustrations were created with BioRender.com. This work was supported by the Leibniz Science Campus (LSC) Living Therapeutic Materials (LifeMat) and DFG Mo2192/4-2.

Open access funding enabled and organized by Projekt DEAL.

Conflicts of Interest

The authors declare no conflict of interest.

Data Availability Statement

The data that support the findings of this study are available from the corresponding author upon reasonable request.

References

1. Y. V. Stepanov, I. Golovynska, S. Golovynskyi, et al., "Red and Near Infrared Light-Stimulated Angiogenesis Mediated via Ca_{2+} Influx, VEGF Production and NO Synthesis in Endothelial Cells in Macrophage or Malignant Environments," *Journal of Photochemistry and Photobiology B: Biology* 227 (2022): 112388, 10.1016/j.jphotobiol.2022.112388.

2. L. Dancáková, T. Vasilenko, I. Kováč, et al., "Low-Level Laser Therapy With 810 Nm Wavelength Improves Skin Wound Healing in Rats With Streptozotocin-Induced Diabetes," *Photomedicine and Laser Surgery* 32, no. 4 (2014): 198–204, 10.1089/pho.2013.3586.

3. A. Medrado, L. S. Pugliese, S. R. A. Reis, and Z. A. Andrade, "Influence of Low Level Laser Therapy on Wound Healing and Its Biological Action

Upon Myofibroblasts," *Lasers in Surgery and Medicine* 32, no. 3 (2003): 239–244, 10.1002/lsm.10126.

4. T. N. Mgwenya, H. Abrahamse, and N. N. Houreld, "Photobiomodulation Studies on Diabetic Wound Healing: An Insight Into the Inflammatory Pathway in Diabetic Wound Healing," *Wound Repair and Regeneration* 33, no. 1 (2025): 13239, 10.1111/wrr.13239.

5. H. J. Lee and Y. K. Kim, "Burn Wound Successfully Treated With 830-nm Light Emitting Diode Phototherapy Combined With Epidermal Growth Factor Solution," *Medical Lasers: Engineeering, Basic Research, and Clinical Applications* 8, no. 2 (2019): 94–96, 10.25289/ML.2019.8.2.94.

6. E. D. S. Carvalho, R. H. Rosa, F. D. M. Pereira, et al., "Effects of Diode Laser Irradiation and Fibroblast Growth Factor on Periodontal Healing of Replanted Teeth After Extended Extra-Oral Dry Time," *Dental Traumatology* 33, no. 2 (2017): 91–99, 10.1111/edt.12308.

7. T. Karpanen, M. Bry, H. M. Ollila, et al., "Overexpression of Vascular Endothelial Growth Factor-B in Mouse Heart Alters Cardiac Lipid Metabolism and Induces Myocardial Hypertrophy," *Circulation Research* 103, no. 9 (2008): 1018–1026, 10.1161/CIRCRESAHA.108.178459.

8. M. Venkatesan, C. Semper, S. Skrivergaard, et al., "Recombinant Production of Growth Factors for Application in Cell Culture," *Iscience* 25, no. 10 (2022): 105054, 10.1016/j.isci.2022.105054.

9. X. Ren, M. Zhao, B. Lash, M. M. Martino, and Z. Julier, "Growth Factor Engineering Strategies for Regenerative Medicine Applications," *Frontiers in Bioengineering and Biotechnology* 7 (2020): 469, 10.3389/fbioe.2019.00469.

10. N. Beheshtizadeh, M. Gharibshahian, M. Bayati, et al., "Vascular Endothelial Growth Factor (VEGF) Delivery Approaches in Regenerative Medicine," *Biomedicine & Pharmacotherapy* 166 (2023): 115301, 10.1016/j.biopha.2023.115301.

11. S. Nazemidashtarjandi, B. Larsen, K. Cheng, et al., "Near-Infrared Light-Responsive Hydrogels for on-Demand Dual Delivery of Proangiogenic Growth Factors," *Acta Biomaterialia* 183 (2024): 61–73, 10.1016/j.actbio.2024.05.052.

12. S. Ma, C. Zhang, X. Ren, et al., "Photothermally Responsive Hydrogel Releases Basic Fibroblast Growth Factor to Promote the Healing of Infected Wounds," *Biomaterials Research* 29 (2025): 0156, 10.34133/bmr.0156.

13. S. Wang, Z. Zhang, S. Wei, et al., "Near-Infrared Light-Controllable MXene Hydrogel for Tunable on-Demand Release of Therapeutic Proteins," *Acta Biomaterialia* 130 (2021): 138–148, 10.1016/j.actbio.2021.05.027.

14. L. Miao, X. Lu, Y. Wei, et al., "Near-Infrared Light-Responsive Nanocomposite Hydrogels Loaded With Epidermal Growth Factor for Diabetic Wound Healing," *Materials Today Bio* 31 (2025): 101578, 10.1016/j.mtbio.2025.101578.

15. L. Wang, N. Wang, W. Zhang, et al., "Therapeutic Peptides: Current Applications and Future Directions," *Signal Transduction and Targeted Therapy* 7, no. 1 (2022): 48, 10.1038/s41392-022-00904-4.

16. M. G. Rizzo, N. Palermo, U. D'Amora, et al., "Multipotential Role of Growth Factor Mimetic Peptides for Osteochondral Tissue Engineering," *International Journal of Molecular Sciences* 23, no. 13 (2022): 7388, 10.3390/ijms23137388.

17. K. Ito, Y. Matsuda, A. Mine, et al., "Single-Chain Tandem Macrocyclic Peptides as a Scaffold for Growth Factor and Cytokine Mimetics," *Communications Biology* 5 (2022): 56, 10.1038/s42003-022-03015-6.

18. Targeting angiogenesis: Structural characterization and biological properties of a de novo engineered VEGF mimicking peptide | PNAS Accessed July 16, 2025, https://www.pnas.org/doi/abs/10.1073/pnas.0505047102.

19. D. Diana, A. Basile, L. De Rosa, et al., "β-Hairpin Peptide That Targets Vascular Endothelial Growth Factor (VEGF) Receptors," *Journal of Biological Chemistry* 286, no. 48 (2011): 41680–41691, 10.1074/jbc.M111.257402.

20. P. Dhakane, V. S. Tadimarri, and S. Sankaran, "Light-Regulated Pro-Angiogenic Engineered Living Materials," *Advanced Functional Materials* 33, no. 31 (2023): 2212695, 10.1002/adfm.202212695.

21. V. S. Tadimarri, M. Blanch-Asensio, K. Deshpande, et al., "PEARL: Protein Eluting Alginate With Recombinant Lactobacilli," *Small* n/a (2025): 2408316, 10.1002/smll.202408316.

22. S. S. Meier, M. Hörzing, C. Böhm, et al., "Engineering NIR-Sighted Bacteria," *Elife* 14 (2025): RP107069, 10.7554/eLife.107069.2.

23. K. J. Downing, R. A. McAdam, and V. Mizrahi, "*Staphylococcus aureus* Nuclease Is a Useful Secretion Reporter for Mycobacteria," *Gene* 239, no. 2 (1999): 293–299, 10.1016/S0378-1119(99)00408-4.

24. A. A. M. Fischer, L. Schatz, J. Baaske, W. Römer, W. Weber, and R. Thuenauer, "Real-Time Monitoring of Cell Surface Protein Arrival With Split Luciferases," *Traffic* 24, no. 10 (2023): 453–462, 10.1111/tra.12908.

25. B. Han, F. L. Hall, and M. E. Nimni, "Refolding of a Recombinant Collagen-Targeted TGF-β2 Fusion Protein Expressed in *Escherichia coli*," *Protein Expression and Purification* 11, no. 2 (1997): 169–178, 10.1006/prep.1997.0784.

26. G. R. M. Kleiner-Grote, J. M. Risse, and K. Friehs, "Secretion of Recombinant Proteins From E. coli," *Engineering in Life Sciences* 18, no. 8 (2018): 532–550, 10.1002/elsc.201700200.

27. M. Gibisch, P. Gorecki, C. Tauer, et al., "Extracellular Peptide Production in Escherichia coli by Inducible Downregulation of Lipoprotein Lpp via MicL sRNA," *Applied Microbiology and Biotechnology* 109, no. 1 (2025): 136, 10.1007/s00253-025-13524-z.

28. S. S. Emani, A. Kan, T. Storms, et al., "Periplasmic Stress Contributes to a Trade-Off between Protein Secretion and Cell Growth in Escherichia coli Nissle 1917," *Synthetic Biology* 8, no. 1 (2023): ysad013, 10.1093/synbio/ysad013.

29. H. Hiemstra, L. Dijkhuizen, and W. Harder, "Diffusion of Oxygen in Alginate Gels Related to the Kinetics of Methanol Oxidation by Immobilized Hansenula Polymorpha Cells," *European Journal of Applied Microbiology and Biotechnology* 18, no. 4 (1983): 189–196, 10.1007/BF00501507.

30. M. Shishido and M. Toda, "Simulation of Oxygen Concentration Profile in Calcium Alginate Gel Beads Entrapping Microbes During Biological Phenol Degradation," *Chemical Engineering Science* 51, no. 6 (1996) 859–872, 10.1016/0009-2509(95)00332-0.

31. S. M. Mavris and L. M. Hansen, "Optimization of Oxygen Delivery Within Hydrogels," *Journal of Biomechanical Engineering* 143, no. 10 (2021): 101004, 10.1115/1.4051119.

32. T. Yoshida and C. T. Migita, "Mechanism of Heme Degradation by Heme Oxygenase," *Journal of Inorganic Biochemistry* 82, no. 1-4 (2000): 33–41, https://doi.org/10.1016/s0162-0134(00)00156-2.

33. M. R. Hamblin, "Mechanisms and Applications of the Anti-Inflammatory Effects of Photobiomodulation," *AIMS Biophysics* 4, no. 3 (2017): 337–361, https://doi.org/10.3934/biophy.2017.3.337.

34. G. K. Keshri, G. Kumar, M. Sharma, K. Bora, B. Kumar, and A. Gupta, "Photobiomodulation Effects of Pulsed-NIR Laser (810 nm) and LED (808 ± 3 nm) With Identical Treatment Regimen on Burn Wound Healing: A Quantitative Label-Free Global Proteomic Approach," *Journal of Photochemistry and Photobiology* 2021;6:100024, https://doi.org/10.1016/j.jpap.2021.100024.

35. IEC 62471:2006.International Electrotechnical Commission, IEC 62471: PhotobiologicalSafety of Lamps and Lamp Systems, (accessed: 2006), https://webstore.iec.ch/en/publication/7076.

36. IEC 60825-1:2014.International Electrotechnical Commission, IEC 60825-1: Safety ofLaser Products—Part 1, (accessed: 2014), https://webstore.iec.ch/en/publication/3587.

37. Y. Kubota, H. K. Kleinman, G. R. Martin, and T. J. Lawley, "Role of Laminin and Basement Membrane in the Morphological Differentiation of Human Endothelial Cells Into Capillary-Like Structures," *The Journal*

of Cell Biology 107, no. 4 (1988): 1589–1598, https://doi.org/10.1083/jcb.107.4.1589.

38. E. Zudaire, L. Gambardella, C. Kurcz, and S. Vermeren, "A Computational Tool for Quantitative Analysis of Vascular Networks," *PLoS One* 6, no. 11 (2011): 27385, https://doi.org/10.1371/journal.pone.0027385.

39. M. N. Nakatsu, R. C. A. Sainson, S. Pérez-del-Pulgar, et al., "VEGF121 and VEGF165 Regulate Blood Vessel Diameter Through Vascular Endothelial Growth Factor Receptor 2 in an In Vitro Angiogenesis Model," *Laboratory Investigation* 83, no. 12 (2003): 1873–1885, https://doi.org/10.1097/01.LAB.0000107160.81875.33.

40. R. Winter, P. Dungel, F. M. J. Reischies, et al., "Photobiomodulation (PBM) Promotes Angiogenesis In-Vitro and in Chick Embryo Chorioallantoic Membrane Model," *Scientific Reports* 8, no. 1 (2018): 17080, https://doi.org/10.1038/s41598-018-35474-5.

41. B. Firouz, L. Faihs, P. Slezak, et al., "Testing the Effects of Photobiomodulation on Angiogenesis in a Newly Established CAM Burn Wound Model," *Scientific Reports* 13, no. 1 (2023): 22985, https://doi.org/10.1038/s41598-023-50165-6.

42. R. G. Frykberg and J. Banks, "Challenges in the Treatment of Chronic Wounds," *Advances in Wound Care* 4, no. 9 (2015): 560–582, https://doi.org/10.1089/wound.2015.0635.

43. E. Colombo, A. Signore, S. Aicardi, et al., "Experimental and Clinical Applications of Red and Near-Infrared Photobiomodulation on Endothelial Dysfunction: A Review," *Biomedicines* 9, no. 3 (2021): 274, https://doi.org/10.3390/biomedicines9030274.

44. C. R. Gurbatri, G. A. Radford, L. Vrbanac, et al., "Engineering Tumor-Colonizing E. coli Nissle 1917 for Detection and Treatment of Colorectal Neoplasia," *Nature Communications* 15, no. 1 (2024): 646, https://doi.org/10.1038/s41467-024-44776-4.

45. M. Alhubail, A. J. McBain, and C. A. O'Neill, "A Survey of Multiple Candidate Probiotic Bacteria Reveals Specificity in the Ability to Modify the Effects of Key Wound Pathogens," *Microbiology Spectrum* 12, no. 6 (2024): e0034724, https://doi.org/10.1128/spectrum.00347-24.

46. M. B. Łabowska, M. Skrodzka, H. Sicińska, I. Michalak, and J. Detyna, "Influence of Cross-Linking Conditions on Drying Kinetics of Alginate Hydrogel," *Gels* 9, no. 1 (2023): 63, https://doi.org/10.3390/gels9010063.

47. J. C. White, M. E. Godsey, and S. R. Bhatia, "Perfluorocarbons Enhance Oxygen Transport in Alginate-Based Hydrogels," *Polymers for Advanced Technologies* 25, no. 11 (2014): 1242–1246, https://doi.org/10.1002/pat.3296.

48. P. Demianenko, B. Minisini, M. Lamrani, and F. Poncin-Epaillard, "How the Structural and Physicochemical Properties of Polyacrylamide/Alginate Hydrogel Influence Its Oxygen Permeability," *Polymer Testing* 53 (2016): 299–304, https://doi.org/10.1016/j.polymertesting.2016.06.015.

49. T. P. Richardson, M. C. Peters, A. B. Ennett, and D. J. Mooney, "Polymeric System for Dual Growth Factor Delivery," *Nature Biotechnology* 19, no. 11 (2001): 1029–1034, https://doi.org/10.1038/nbt1101-1029.

50. R. R. Chen, E. A. Silva, W. W. Yuen, and D. J. Mooney, "Spatio–Temporal VEGF and PDGF Delivery Patterns Blood Vessel Formation and Maturation," *Pharmaceutical Research* 24, no. 2 (2007): 258–264, https://doi.org/10.1007/s11095-006-9173-4.

51. D. Ribatti, "The Chick Embryo Chorioallantoic Membrane as an In Vivo Assay to Study Antiangiogenesis," *Pharmaceuticals* 3, no. 3 (2010): 482–513, https://doi.org/10.3390/ph3030482.

52. P. Nowak-Sliwinska, T. Segura, and M. L. Iruela-Arispe, "The Chicken Chorioallantoic Membrane Model in Biology, Medicine and Bioengineering," *Angiogenesis* 17, no. 4 (2014): 779–804, https://doi.org/10.1007/s10456-014-9440-7.

53. B. Stüven, R. Stabel, R. Ohlendorf, J. Beck, R. Schubert, and A. Möglich, "Characterization and Engineering of Photoactivated Adenylyl Cyclases," *Biological Chemistry* 400, no. 3 (2019): 429–441, https://doi.org/10.1515/hsz-2018-0375.

54. A. Möglich, "An Open-Source, Cross-Platform Resource for Nonlinear Least-Squares Curve Fitting," *Journal of Chemical Education* 95, no. 12 (2018): 2273–2278, https://doi.org/10.1021/acs.jchemed.8b00649.

55. E. Multamäki, A. García de Fuentes, O. Sieryi, et al., "Optogenetic Control of Bacterial Expression by Red Light," *ACS Synthetic Biology* 11, no. 10 (2022): 3354–3367, https://doi.org/10.1021/acssynbio.2c00259.

Supporting Information

Additional supporting information can be found online in the Supporting Information section.

Supporting File: adfm74944-sup-0001-SuppMat.pdf.

Supplemental Movie adfm74944-sup-0002-MovieS1.avi.

Supplemental Movie adfm74944-sup-0003-MovieS2.mp4.

Supplemental Movie adfm74944-sup-0004-MovieS3.mp4.